Acta Mech 226, 2807–2829 (2015)
DOI 10.1007/s00707-015-1351-1

ORIGINAL PAPER

Y. Z. Chen

Numerical solution for a crack embedded in multiple elliptic layers with different elastic properties

Received: 29 December 2014 / Revised: 17 February 2015 / Published online: 14 April 2015

Abstract The medium is composed of an elliptic inclusion and many confocal elliptic layers. The crack is embedded in the elliptic inclusion. The remote loading is applied at the remote place of the matrix. Complex variable method and conformal mapping are used to study the mentioned problem. This paper provides a numerical solution for the mentioned crack problem. The continuity condition for the traction and displacement along the interface is reduced to a relation of two sets of Laurent series coefficients for the complex potentials defined in the interior or exterior to the interface. This formulation is called the matrix transfer method in this paper. From the following three conditions, the traction-free condition along creak face, the continuity condition for the traction and displacement along the interfaces and the remote loading condition, the problem is finally solved. Servable numerical examples are provided. For the exterior finite matrix case, the relevant solution is also provided.

1 Introduction

In an earlier year, Eshelby [1] studied the eigenstrain problem. It was proved that the elastic field in an ellipsoidal inclusion is also uniform if the uniform eigenstrains are applied in an inclusion. Later Mura [2] studied the inclusion problem in more detail. He suggested that inclusions can be categorized into (i) inhomogeneities, (ii) homogeneous inclusions and (iii) inhomogeneous inclusions.

Studies in the field of inhomogeneities and inclusions are numerous [3–11]. We only cite a portion of them. A problem with three-phase elliptic inclusion in antiplane shear was studied [4]. It was proved that the stresses within a multiphase elliptic inclusion are uniform provided that all interfaces consist of confocal ellipses. The existence of a uniform hydrostatic stress state inside an arbitrary-shape (non-elliptical) inclusion bonded by an interphase layer to an infinite elastic matrix subjected to remote uniform in-plane stresses is studied [5]. The null-field integral equation for an infinite medium containing circular holes and/or inclusions was derived. Using the suggested null-field integral equation, the multi-inclusion problem under antiplane shear was solved numerically [6].

Based on a complex variable boundary integral equation (CVBIE) suggested previously, a numerical solution for the elastic inclusion problem using CVBIE was provided [7]. For a finite plate containing two dissimilar inclusions, the boundary value problem for a finite plate containing two dissimilar inclusions was solved by using the CVBIE [8].

A review of recent works on inclusions was proposed [9]. The problems of a single inclusion, two inclusions, and multiple inclusions, dislocations and cracks as well as various methods used to address these problems are discussed. The review concludes with an outlook on future research directions.

Y. Z. Chen (✉)
Division of Engineering Mechanics, Jiangsu University, Zhenjiang, 212013 Jiangsu, People's Republic of China
E-mail: chens@ujs.edu.cn
Tel.: 086 511 88780780

The problem of a confocally multicoated elliptical inclusion in an unbounded matrix subjected to an antiplane shear was studied [10]. For the Eshelby's elliptic inclusion in antiplane elasticity, a closed-form solution was provided [11]. In the formulation, the prescribed eigenstrains are not only for the uniform distribution, but also for the linear form.

Some researchers studied the crack problem for the crack outside of the inclusion. The interaction problem between a circular inclusion and a symmetrically branched crack embedded in an infinite elastic medium is solved [12]. By using the new integral equation method, the solution for the problem of a two-dimensional infinite isotropic medium with various inclusions and cracks was presented [13]. A curved crack problem for an infinite plate containing an elastic inclusion is considered [14]. A fundamental solution is proposed, which corresponds to the stress field caused by a point dislocation in an infinite plate containing an elastic inclusion. The solution to a curved matrix crack interacting with a circular elastic inclusion is presented [15]. The problem is formulated using the Kolosov–Muskhelishvili complex stress potential technique [16].

A crack problem in a confocal elliptic inhomogeneity embedded in an infinite medium was studied [17]. Plane and antiplane solutions associated with remote loading conditions are obtained.

In the present study, the medium is composed of an elliptic inclusion and many confocal elliptic layers. The crack is embedded in the elliptic inclusion. The remote loading is applied at the remote place of matrix. Complex variable method and conformal mapping are used to study the mentioned problem [16]. This paper provides a numerical solution for the mentioned crack problem.

All complex potentials in the mapping plane are expressed in the form of Laurent series. In a weaker formulation, the traction-free condition along the crack is reduced to a relation between coefficients of Laurent series for two complex potentials. In addition, the continuity condition for the traction and displacement along the interface is reduced to a relation of two sets of Laurent series coefficients for the complex potentials, which are the interior or exterior to the interface. This formulation is called the matrix transfer method in this paper. Finally, from the loading condition at the remote place, all complex potentials defined on layers can be evaluated. In addition, the stress intensity factor at the crack tip can be evaluated. The stress distributions along the both sides of interfaces are also presented in the study. Several numerical examples are provided in the paper.

Previously, we studied the problem for multiply confocal layers with dissimilar elastic properties [18]. In that paper, the matrix transfer method was suggested. Therefore, the relation between two layers is the same as used in the present paper. However, the perfect inclusion is assumed in [18], and a crack is embedded in the inclusion in the present study. Therefore, the matrix transfer method itself cannot provide the final solution in the present paper.

2 Analysis

2.1 Some basic equations in complex variable method in plane elasticity

The following analysis depends on the complex variable function method in plane elasticity [16]. In the method, the stresses $(\sigma_x, \sigma_y, \sigma_{xy})$, the resultant forces (X, Y) and the displacements (u, v) are expressed in terms of two complex potentials $\phi_*(z)$ and $\psi_*(z)$ such that

$$\begin{aligned} \sigma_x + \sigma_y &= 4Re\phi'_*(z), \\ \sigma_y - \sigma_x + 2i\sigma_{xy} &= 2[\bar{z}\phi''_*(z) + \psi'_*(z)], \end{aligned} \tag{1}$$

$$F = -Y + iX = \phi_*(z) + z\overline{\phi'_*(z)} + \overline{\psi_*(z)}, \tag{2}$$

$$2G(u + iv) = \kappa\phi_*(z) - z\overline{\phi'_*(z)} - \overline{\psi_*(z)}, \tag{3}$$

where $z = x + iy$ denotes a complex variable, G is the shear modulus of elasticity, $\kappa = (3 - \nu)/(1 + \nu)$ is for the plane stress problems, $\kappa = 3 - 4\nu$ is for the plane strain problems, and ν is Poisson's ratio. In the present study, the plane strain condition is assumed thoroughly. In the following, we occasionally rewrite the displacements "u," "v" as u_1, u_2, $\sigma_x, \sigma_y, \sigma_{xy}$ as $\sigma_{11}, \sigma_{22}, \sigma_{12}$ and "x," "y" as x_1, x_2, respectively.

In the analysis, we use the following conformal mapping [16] (Fig. 1):

$$z = \omega(\varsigma) = R\left(\varsigma + \frac{m}{\varsigma}\right), \text{ with } R = \frac{a+b}{2}, \quad m = \frac{a-b}{a+b}, \tag{4}$$

$$\omega'(\varsigma) = R\left(1 - \frac{m}{\varsigma^2}\right), \quad \omega''(\varsigma) = \frac{2Rm}{\varsigma^3}. \tag{5}$$

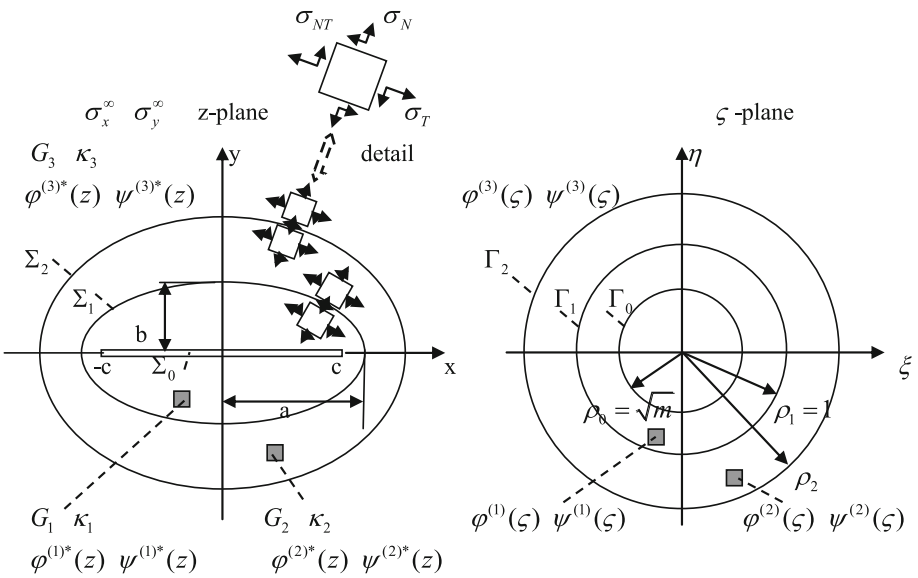

Fig. 1 Mapping relations: (a) the finite elliptic inclusion with two half-axes "a" and "b," with a crack $(-c, c)$ with $c = \sqrt{a^2 - b^2}$ (in the z-plane) and elastic constants G_1, κ_1 mapped into the ring region $\sqrt{m} < |\varsigma| \le 1$ [in the ς-plane with $m = (a-b)/(a+b)$], (b) the elliptic layer bounded by two interfaces Σ_1 and Σ_2 (in the z-plane) with elastic constants G_2, κ_2 mapped into a ring region bounded by two circles Γ_1 and Γ_2, or $\rho_1 \le |\varsigma| \le \rho_2$ with $\rho_1 = 1$ (in the ς-plane), (c) the infinite matrix region exterior to the interface Σ_2 (in the z-plane) with elastic constants G_3, κ_3 mapped into the infinite region exterior to circle Γ_2, or $|\varsigma| \ge \rho_2$ (in the ς-plane)

The mapping function maps the exterior region of a unite circle in the ς-plane to the elliptic contour with two half-axes "a" and " b" in the z-plane. In addition, this mapping function also maps the ring region defined by $\sqrt{m} < |\varsigma| \le 1$ in the ς-plane to the finite elliptic region with a cut interval $(-c, c)$ $(c = \sqrt{a^2 - b^2})$ in the z-plane (Fig. 1).

The inversion of the mapping $z = \omega(\varsigma)$ is defined by

$$\varsigma = \Omega(z) = \frac{z + \sqrt{z^2 - 4mR^2}}{2R}. \tag{6}$$

In the following analysis, we denote

$$\phi(\varsigma) = \phi_*(z)\,|_{z=\omega(\varsigma)}, \quad \psi(\varsigma) = \psi_*(z)\,|_{z=\omega(\varsigma)}. \tag{7}$$

Clearly, after using the mentioned conformal mapping, from Eqs. (1) to (3) we have

$$\begin{aligned} \sigma_x + \sigma_y &= 4Re\frac{\phi'(\varsigma)}{\omega'(\varsigma)}, \\ \sigma_y - \sigma_x + 2i\sigma_{xy} &= 2\left(\frac{\overline{\omega(\varsigma)}(\phi''(\varsigma)\omega'(\varsigma) - \phi'(\varsigma)\omega''(\varsigma))}{(\omega'(\varsigma))^3} + \frac{\psi'(\varsigma)}{\omega'(\varsigma)}\right), \end{aligned} \tag{8}$$

$$F = -Y + iX = \phi(\varsigma) + \omega(\varsigma)\frac{\overline{\phi'(\varsigma)}}{\omega'(\varsigma)} + \overline{\psi(\varsigma)}, \tag{9}$$

$$2G(u + iv) = \kappa\phi(\varsigma) - \omega(\varsigma)\frac{\overline{\phi'(\varsigma)}}{\omega'(\varsigma)} - \overline{\psi(\varsigma)}. \tag{10}$$

From Eqs. (8) to (10) we see that, if one obtains the complex potentials $\phi(\varsigma)$ and $\psi(\varsigma)$ in the mapping plane, one can get the stress and displacement in the physical plane.

2.2 Relation derived from traction-free condition along the crack face

In the study, the whole region is composed of three-phase composites: (i) the elliptic inclusion with a crack with the elastic constants G_1, κ_1, (ii) the elliptic layer bound by two interfaces Σ_1 and Σ_2 with the elastic constants G_2, κ_2, and (iii) the infinite matrix exterior to the interface Σ_2 with the elastic constants G_3, κ_3. In addition, the remote tensions σ_x^{∞} and σ_y^{∞} are applied at infinity (Fig. 1).

The elliptic inclusion with the elastic constants G_1, κ_1 has two half-axes "a" and "b" (Fig. 1). In addition, a crack $(-c, c)$ $(c = \sqrt{a^2 - b^2})$ is embedded in the inclusion. The assumed complex potentials in the inclusion region are denoted by $\phi^{(1)*}(z)$ and $\psi^{(1)*}(z)$. After using conformal mapping shown by Eq. (4), we can define the relevant complex potentials in the mapping plane as follows:

$$\phi^{(1)}(\varsigma) = \phi^{(1)*}(z)\mid_{z=\omega(\varsigma)}, \quad \psi^{(1)}(\varsigma) = \psi^{(1)*}(z)\mid_{z=\omega(\varsigma)}, \quad (\sqrt{m} < |\varsigma| \le 1). \tag{11}$$

In addition, since the elliptic plate with two half-axes "a" and "b" and the crack line $(-c, c)$ (in the z-plane) maps into the ring region $\sqrt{m} < |\varsigma| \le 1$(in the ς-plane), two complex potentials can be expressed in the following Laurent series form:

$$\phi^{(1)}(\varsigma) = \sum_{k=-N}^{N}{}' a_k^{(1)} \varsigma^k, \quad \psi^{(1)}(\varsigma) = \sum_{k=-N}^{N}{}' b_k^{(1)} \varsigma^k \quad (\sqrt{m} < |\varsigma| \le 1). \tag{12}$$

In Eq. (12), "N" denotes the terms truncated in the derivation and computation. Because of no influence for the term of $k = 0$ in Eq. (12) for the continuity condition along the interface, in $\sum_{k=-N}^{N}{}'$ the prime means that the term $k = 0$ has been excluded in the summation.

In fact, in the case of many confocal elliptic layers and symmetry loading with respect to two axes "ox" and "oy," the even terms in complex potentials $\phi^{(1)}(\varsigma)$ and $\psi^{(1)}(\varsigma)$ do not exist. However, if the applied loading on the exterior layer is only symmetric with respect to the axis "ox," both the odd and even terms exist in the mentioned complex potentials. For the complex potentials shown by Eq. (12), we design the form of those complex potentials which can be used to a general loading condition.

From a general analysis in the fracture mechanics, the complex potentials $\phi^{(1)*\prime}(z)$, $\psi^{(1)*\prime}(z)$ are singular at the points $z = c$ and $z = -c$. Alternatively speaking, $\phi^{(1)'}(\varsigma)/\omega'(\varsigma)(= \phi^{(1)*\prime}(z))$ and $\psi^{(1)'}(\varsigma)/\omega'(\varsigma)(= \psi^{(1)*\prime}(z))$ are singular at the points $\varsigma = \sqrt{m}$ and $\varsigma = -\sqrt{m}$.

From Eqs. (2) and (4), the traction-free condition along the crack face is as follows:

$$\phi^{(1)}(\varsigma) + \frac{\omega(\varsigma)}{\overline{\omega'(\varsigma)}}\overline{\phi'^{(1)}(\varsigma)} + \overline{\psi^{(1)}(\varsigma)} = 0, \quad \left(\varsigma \in \Gamma_o, \text{ with } \varsigma = \sqrt{m}e^{i\theta}\right) \tag{13}$$

or

$$\phi^{(1)}(\varsigma) + \frac{\omega(\varsigma)}{\overline{\omega'(\varsigma)}}\overline{\phi'^{(1)}(\varsigma)} = -\overline{\psi^{(1)}(\varsigma)}, \quad \left(\varsigma \in \Gamma_o, \text{ with } \varsigma = \sqrt{m}e^{i\theta}\right). \tag{14}$$

From Eq. (14), we see that two complex potentials $\phi^{(1)}(\varsigma)$ and $\psi^{(1)}(\varsigma)$ are not independent. The equality shown by Eq. (14) can be satisfied in a weaker form. To this end, we can apply the following operator:

$$\frac{1}{2\pi i}\int_{\Gamma_0}[\ldots]\varsigma^{j-1}\mathrm{d}\varsigma \quad (j = -N, -(N-1), \ldots, -2, -1, 1, 2, \ldots, N-1, N) \tag{15}$$

to both sides of Eq. (14). After performing this operation, we have

$$[\mathbf{K}_1]_{2\mathbf{N}\times 2\mathbf{N}}\{A_{1p}\}_{2N} = [\mathbf{K}_2]_{2\mathbf{N}\times 2\mathbf{N}}\{A_{1q}\}_{2N} \tag{16}$$

where the two vectors are defined by

$$\{A_{1p}\}_{2N} = \left\{a_{-N}^{(1)}a_{-(N-1)}^{(1)}\cdots a_{-1}^{(1)}a_1^{(1)}\cdots a_{N-1}^{(1)}a_N^{(1)}\right\}^{\mathrm{T}}, \tag{17}$$

$$\{A_{1q}\}_{2N} = \left\{b_{-N}^{(1)}b_{-(N-1)}^{(1)}\cdots b_{-1}^{(1)}b_1^{(1)}\cdots b_{N-1}^{(1)}b_N^{(1)}\right\}^{\mathrm{T}}. \tag{18}$$

For evaluating all elements in the matrices $[\mathbf{K}_1]_{2\mathbf{N}\times 2\mathbf{N}}$ and $[\mathbf{K}_2]_{2\mathbf{N}\times 2\mathbf{N}}$, we can refer to some results in "Appendix A."

From Eq. (16), we have

$$\{A_{1q}\}_{2N} = [\mathbf{G}]_{2\mathbf{N}\times 2\mathbf{N}}\{A_{1p}\}_{2N} \tag{19}$$

where

$$[\mathbf{G}]_{2\mathbf{N}\times 2\mathbf{N}} = [\mathbf{K}_2^{-1}]_{2\mathbf{N}\times 2\mathbf{N}}[\mathbf{K}_1]_{2\mathbf{N}\times 2\mathbf{N}}. \tag{20}$$

From Eqs. (17), (18) and (19), we have

$$\{A_1\}_{4N} = [\mathbf{H}]_{4\mathbf{N}\times 2\mathbf{N}}\{A_{1p}\}_{2N} \tag{21}$$

where

$$[\mathbf{H}]_{4\mathbf{N}\times 2\mathbf{N}} = \begin{matrix}[\mathbf{I}]_{2\mathbf{N}\times 2\mathbf{N}} \\ [\mathbf{G}]_{2\mathbf{N}\times 2\mathbf{N}}\end{matrix}, \tag{22}$$

$$\{A_1\}_{4N} = \left\{a_{-N}^{(1)}a_{-(N-1)}^{(1)}\cdots a_{-1}^{(1)}a_1^{(1)}\cdots a_{N-1}^{(1)}a_N^{(1)}\ b_{-N}^{(1)}b_{-(N-1)}^{(1)}\cdots b_{-1}^{(1)}b_1^{(1)}\cdots b_{N-1}^{(1)}b_N^{(1)}\right\}^{\mathrm{T}}. \tag{23}$$

In Eq. (22), $[\mathbf{I}]_{2\mathbf{N}\times 2\mathbf{N}}$ denotes the unit diagonal matrix.

2.3 Evaluation of the transfer matrix from the continuity condition along the interface

The elliptic layer with the elastic constants G_2, κ_2 is bound by the interfaces Σ_1 and Σ_2 (in the z-plane). Clearly, the two elliptic interfaces Σ_1 and Σ_2 are confocal. After using the conformal mapping, the layer is mapped on the ring region bound by two circles Γ_1 and Γ_2(in the ς-plane) (Fig. 1). In addition, two circles Γ_1 and Γ_2 have the relevant radius $\rho_1 = 1$ and ρ_2, respectively.

The assumed complex potentials in the layer are denoted by $\phi^{(2)*}(z)$ and $\psi^{(2)*}(z)$. After using conformal mapping shown by Eq. (4), we can define the relevant complex potentials in the mapping plane as follows:

$$\phi^{(2)}(\varsigma) = \phi^{(2)*}(z)\mid_{z=\omega(\varsigma)}, \quad \psi^{(2)}(\varsigma) = \psi^{(2)*}(z)\mid_{z=\omega(\varsigma)}. \tag{24}$$

Similarly, two complex potentials can be expressed in the Laurent series form

$$\phi^{(2)}(\varsigma) = {\sum_{k=-N}^{N}}' a_k^{(2)}\varsigma^k, \quad \psi^{(2)}(\varsigma) = {\sum_{k=-N}^{N}}' b_k^{(2)}\varsigma^k \quad (\rho_1 \le |\varsigma| \le \rho_2). \tag{25}$$

A similar notation $\sum_{k=-N}^{N}{}'$ used in Eq. (12) is used for Eq. (25).

The infinite matrix with the elastic constants G_3, κ_3 is located outside the interface Σ_2 (in z-plane). After using the conformal mapping, the matrix is mapped on the region outside to the circle Γ_2 with the radius ρ_2 (in the ς-plane) (Fig. 1).

The assumed complex potentials in the matrix are denoted by $\phi^{(3)*}(z)$ and $\psi^{(3)*}(z)$. After using conformal mapping shown by Eq. (4), we can define the relevant complex potentials in the mapping plane as follows:

$$\phi^{(3)}(\varsigma) = \phi^{(3)*}(z)\mid_{z=\omega(\varsigma)}, \quad \psi^{(3)}(\varsigma) = \psi^{(3)*}(z)\mid_{z=\omega(\varsigma)}. \tag{26}$$

Similarly, two complex potentials can be expressed in the Laurent series form

$$\phi^{(3)}(\varsigma) = {\sum_{k=-N}^{N}}' a_k^{(3)}\varsigma^k, \quad \psi^{(3)}(\varsigma) = {\sum_{k=-N}^{N}}' b_k^{(3)}\varsigma^k \qquad (|\varsigma| \ge \rho_2). \tag{27}$$

A similar notation for $\sum_{k=-N}^{N}{}'$ used in Eq. (12) is used for Eq. (27). In the present study, all the coefficients, or $a_k^{(1)}, b_k^{(1)}, a_k^{(2)}, \quad b_k^{(2)}a_k^{(3)}, b_k^{(3)}(k = -N, -(N-1), \ldots, -1, 1, 2, \ldots, N)$ in the assumed complex potentials take a real value.

In the case of the remote loading σ_x^∞, σ_y^∞, the complex potentials in the matrix portion can be expressed as [16]

$$\phi^{(3)*}(z) = h_1 z + \sum_{k=-N}^{-1} p_k^{(3)} z^k, \quad \psi^{(3)*}(z) = h_2 z + \sum_{k=-N}^{-1} q_k^{(3)} z^k \tag{28}$$

where $p_k^{(3)}$ and $q_k^{(3)}$ are some undetermined coefficients, and h_1, h_2 are defined by

$$h_1 = \frac{\sigma_x^\infty + \sigma_y^\infty}{4}, \qquad h_2 = \frac{\sigma_y^\infty - \sigma_x^\infty}{2}. \tag{29}$$

Naturally, the continuity conditions for displacements and tractions [see below Eqs. (32) and (33)] can be satisfied with a difference of a constant. Therefore, the term of the constant is not included in Eqs. (27) and (28).

After using conformal mapping shown by Eq. (4), from Eqs. (28) and (29), we can define the relevant complex potentials in the mapping plane as follows:

$$\phi^{(3)}(\varsigma) = h_1 R\varsigma + \sum_{k=-N}^{-1} a_k^{(3)} \varsigma^k, \quad \psi^{(3)}(\varsigma) = h_2 R\varsigma + \sum_{k=-N}^{-1} b_k^{(3)} \varsigma^k, \quad (|\varsigma| \geq \rho_2). \tag{30}$$

Comparing Eq. (27) with (30), we see the following relations:

$$\begin{aligned} a_1^{(3)} &= h_1 R, \quad a_k^{(3)} = 0 \quad (\text{for } k \geq 2)\,, \\ b_1^{(3)} &= h_2 R, \quad b_k^{(3)} = 0 \quad (\text{for } k \geq 2). \end{aligned} \tag{31}$$

Physically, Eq. (31) represents the condition for the applied remote loading σ_x^∞ and σ_y^∞.

Without losing generality, we consider the continuity condition for traction and displacement along the interface Σ_1 (Fig. 1). Since the resultant force function and the displacement should be continuous along the interface, from Eqs. (9) and (10) we have

$$\phi^{(1)}(\varsigma) + \frac{\omega(\varsigma)}{\overline{\omega'(\varsigma)}} \overline{\phi'^{(1)}(\varsigma)} + \overline{\psi^{(1)}(\varsigma)} = \phi^{(2)}(\varsigma) + \frac{\omega(\varsigma)}{\overline{\omega'(\varsigma)}} \overline{\phi'^{(2)}(\varsigma)} + \overline{\psi^{(2)}(\varsigma)}, \quad (\varsigma \in \Gamma_1)\,, \tag{32}$$

$$\frac{1}{2G_1}\left\{\kappa_1 \phi^{(1)}(\varsigma) - \frac{\omega(\varsigma)}{\overline{\omega'(\varsigma)}} \overline{\phi'^{(1)}(\varsigma)} - \overline{\psi^{(1)}(\varsigma)}\right\} = \frac{1}{2G_2}\left\{\kappa_2 \phi^{(2)}(\varsigma) - \frac{\omega(\varsigma)}{\overline{\omega'(\varsigma)}} \overline{\phi'^{(2)}(\varsigma)} - \overline{\psi^{(2)}(\varsigma)}\right\}, \quad (\varsigma \in \Gamma_1)\,. \tag{33}$$

It is seen that the continuation conditions shown by Eqs. (32) and (33) are expressed in the continuous form, which is formulated along the interface $\varsigma \in \Gamma_1$ with $\varsigma = \rho_1 e^{i\theta}$ (Fig. 1). Now we want to convert two conditions into a discrete form. To this end, we can apply the following operator:

$$\frac{1}{2\pi i} \int_{\Gamma_1} \{\ldots\} \varsigma^{j-1} \mathrm{d}\varsigma, \quad (j = -N, -(N-1), \ldots, -2, -1, 1, 2, \ldots, N-1, N) \tag{34}$$

to both side of Eqs. (32) and (33). After making the mentioned operation, from Eqs. (32) and (33) we will obtain the following transfer matrix relation:

$$\{A_2\}_{4N} = [\mathbf{S}_{21}]_{4\mathbf{N}\times 4\mathbf{N}} \{A_1\}_{4N} \tag{35}$$

where the two vectors are defined by

$$\{A_1\}_{4N} = \{a_{-N}^{(1)}\, a_{-(N-1)}^{(1)} \cdots a_{-1}^{(1)}\, a_1^{(1)} \cdots a_{N-1}^{(1)}\, a_N^{(1)}\, b_{-N}^{(1)}\, b_{-(N-1)}^{(1)} \cdots b_{-1}^{(1)}\, b_1^{(1)} \cdots b_{N-1}^{(1)}\, b_N^{(1)}\}^{\mathrm{T}}, \tag{36}$$

$$\{A_2\}_{4N} = \{a_{-N}^{(2)}\, a_{-(N-1)}^{(2)} \cdots a_{-1}^{(2)}\, a_1^{(2)} \cdots a_{N-1}^{(2)}\, a_N^{(2)}\, b_{-N}^{(2)}\, b_{-(N-1)}^{(2)} \cdots b_{-1}^{(2)}\, b_1^{(2)} \cdots b_{N-1}^{(2)}\, .b_N^{(2)}\}^{\mathrm{T}}. \tag{37}$$

The matrix $[\mathbf{S}_{21}]_{4\mathbf{N}\times 4\mathbf{N}}$ is called the transfer matrix, which provides a relation between the two vectors $\{A_1\}_{4N}$ and $\{A_2\}_{4N}$.

For evaluating all elements in the matrices $[\mathbf{S}_{21}]_{4\mathbf{N}\times 4\mathbf{N}}$, we can refer to some results in "Appendix A."

Similarly, after using the continuity conditions for traction and displacement along the interface Γ_2 (Fig. 1), we have

$$\{A_3\}_{4N} = [\mathbf{S}_{32}]_{4\mathbf{N}\times 4\mathbf{N}}\{A_2\}_{4N} \tag{38}$$

where

$$\{A_3\}_{4N} = \left\{a_{-N}^{(3)}\, a_{-(N-1)}^{(3)} \cdots a_{-1}^{(3)}\, a_1^{(3)} \cdots a_{N-1}^{(3)}\, a_N^{(3)}\, b_{-N}^{(3)}\, b_{-(N-1)}^{(3)} \cdots b_{-1}^{(3)}\, a_1^{(3)} \cdots b_{N-1}^{(3)}\, b_N^{(3)}\right\}^{\mathrm{T}}. \tag{39}$$

After linking Eqs. (35) and (38) together, we will find

$$\{A_3\}_{4N} = [\mathbf{S}_{31}]_{4\mathbf{N}\times 4\mathbf{N}}\,\{A_1\}_{4N} \tag{40}$$

where

$$[\mathbf{S}_{31}]_{4\mathbf{N}\times 4\mathbf{N}} = [\mathbf{S}_{32}]_{4\mathbf{N}\times 4\mathbf{N}}\,[\mathbf{S}_{21}]_{4\mathbf{N}\times 4\mathbf{N}}. \tag{41}$$

The obtained matrices $[\mathbf{S}_{21}]_{4\mathbf{N}\times 4\mathbf{N}}$, $[\mathbf{S}_{32}]_{4\mathbf{N}\times 4\mathbf{N}}$ and $[\mathbf{S}_{31}]_{4\mathbf{N}\times 4\mathbf{N}}$ (=$[\mathbf{S}_{32}]_{4\mathbf{N}\times 4\mathbf{N}}\,[\mathbf{S}_{21}]_{4\mathbf{N}\times 4\mathbf{N}}$) are called the transfer matrix hereafter. The idea for the formulation of transfer matrix in the antiplane shear problem was also suggested earlier [10]. For the problem of multiple elliptic layers in plane elasticity, the transfer matrix method was suggested in [18,19].

As stated previously, there is a relation between the two vectors $\{A_1\}_{4N}$ and $\{A_{1p}\}_{2N}$ shown by $\{A_1\}_{4N} = [\mathbf{H}]_{4\mathbf{N}\times 2\mathbf{N}}\,\{A_{1p}\}_{2N}$ in Eq. (21). By using this relation and Eqs. (35) and (40), we have

$$\{A_2\}_{4N} = [\mathbf{T}_{21}]_{4\mathbf{N}\times 2\mathbf{N}}\,\{A_{1p}\}_{2N}, \tag{42}$$

$$\{A_3\}_{4N} = [\mathbf{T}_{31}]_{4\mathbf{N}\times 2\mathbf{N}}\,\{A_{1p}\}_{2N} \tag{43}$$

where

$$[\mathbf{T}_{21}]_{4\mathbf{N}\times 2\mathbf{N}} = [\mathbf{S}_{21}]_{4\mathbf{N}\times 4\mathbf{N}}\,[\mathbf{H}]_{4\mathbf{N}\times 2\mathbf{N}}, \tag{44}$$

$$[\mathbf{T}_{31}]_{4\mathbf{N}\times 2\mathbf{N}} = [\mathbf{S}_{31}]_{4\mathbf{N}\times 4\mathbf{N}}\,[\mathbf{H}]_{4\mathbf{N}\times 2\mathbf{N}}. \tag{45}$$

From the above derivation, we see that if the vector $\{A_{1p}\}_{2N}$ is evaluated from a numerical solution, the solution for the three vectors $\{A_1\}_{4N}$, $\{A_2\}_{4N}$ and $\{A_3\}_{4N}$ by using Eqs. (21), (42) and (43), respectively, is obtained.

2.4 Reduction in the transfer matrix from the properties of the complex potentials in the matrix and solution of the problem

For solving the problem, we should use the particular property for the vector $\{A_3\}_{4N}$ shown by Eq. (39). The mentioned property is as follows: $a_1^{(3)} = h_1 R$, $a_k^{(3)} = 0$ (for $k \geq 2$), $b_1^{(3)} = h_2 R$, $b_k^{(3)} = 0$ (for $k \geq 2$).

In Eq. (43), we can preserve some lines for positive power in the Laurent series expansion in the matrix $[\mathbf{T}_{31}]_{4\mathbf{N}\times 2\mathbf{N}}$ and delete those lines for negative power, and obtain

$$\{A_{3p}\}_{2N} = [\mathbf{R}_{31}]_{2\mathbf{N}\times 2\mathbf{N}}\,\{A_{1p}\}_{2N} \tag{46}$$

where

$$\{A_{3p}\}_{2N} = \left\{a_1^{(3)} \cdots a_{N-1}^{(3)}\, a_N^{(3)}\, b_1^{(3)} \cdots b_{N-1}^{(3)} b_N^{(3)}\right\}^{\mathrm{T}}. \tag{47}$$

Note that the matrix $[\mathbf{R}_{31}]_{2\mathbf{N}\times 2\mathbf{N}}$ is obtained from the matrix $[\mathbf{T}_{31}]_{4\mathbf{N}\times 2\mathbf{N}}$ by using the above-mentioned property shown by Eq. (31).

We prefer to write Eq. (46) in the form

$$[\mathbf{R}_{31}]_{2\mathbf{N}\times 2\mathbf{N}}\,\{A_{1p}\}_{2N} = \{A_{3p}\}_{2N}. \tag{48}$$

Clearly, Eq. (48) represents an algebraic equation for the unknown $\{A_{1p}\}_{2N}$ ($\{A_{1p}\}_{2N} = \{a_{-N}^{(1)}\, a_{-(N-1)}^{(1)} \cdots a_{-1}^{(1)}\, a_1^{(1)} \cdots a_{N-1}^{(1)}\, a_N^{(1)}\}^{\mathrm{T}}$). In addition, $\{A_{3p}\}_{2N}$ ($\{A_{3p}\}_{2N} = \{a_1^{(3)} \cdots a_{N-1}^{(3)}\, a_N^{(3)}\, b_1^{(3)} \cdots b_{N-1}^{(3)}\, b_N^{(3)}\}^{\mathrm{T}}$) represents the right-hand term. Substituting $a_1^{(3)} = h_1 R$, $a_k^{(3)} = 0$ $b_1^{(3)} = h_2 R$, $b_k^{(3)} = 0$ (for $k \geq 2$) [from

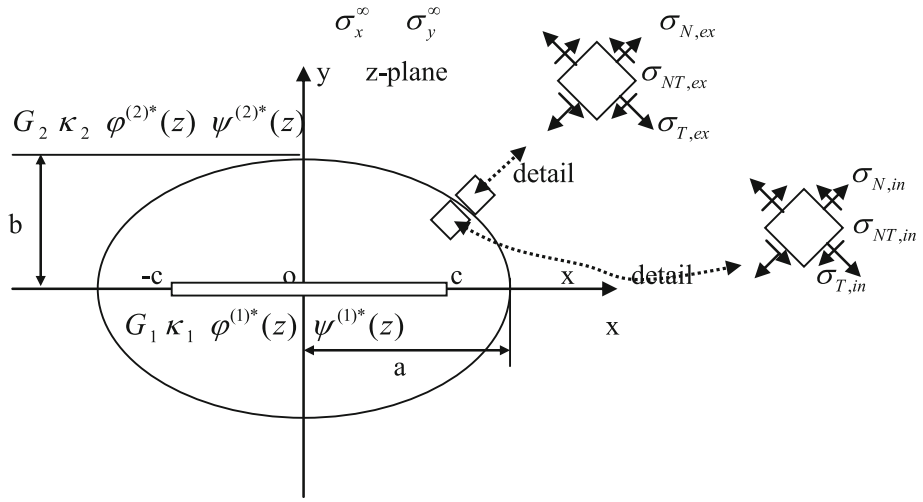

Fig. 2 An elliptic inclusion with a crack $(-c, c)$ $c = \sqrt{a^2 - b^2}$ with elastic constants G_1, κ_1 embedded in the infinite matrix with elastic constants G_2, κ_2

the condition (31)] in the vector $\{A_{3p}\}_{2N}$ shown by Eq. (47) and solving the algebraic equation shown by Eq. (48), we can get a solution for $\{A_{1p}\}_{2N}$.

As stated previously, after the vector $\{A_{1p}\}_{2N}$ is evaluated from the numerical solution for Eq. (48), we can obtain the solution for the three vectors $\{A_1\}_{4N}$, $\{A_2\}_{4N}$ and $\{A_3\}_{4N}$ by using Eqs. (21), (42) and (43), respectively. Alternatively speaking, we obtain a numerical solution for the complex potentials $\phi^{(1)}(\varsigma)$, $\psi^{(1)}(\varsigma)\phi^{(2)}(\varsigma)$, $\psi^{(2)}(\varsigma)$, $\phi^{(3)}(\varsigma)$, $\psi^{(3)}(\varsigma)$, respectively.

Finally, we can evaluate the stress intensity factor (SIF) at the crack tip by [19]

$$K_1 = 2\sqrt{2\pi(z-c)}\,\phi^{(1)*\prime}(z)\,|_{z\to c} = 2\sqrt{2\pi(\omega(\varsigma)-c)}\,\phi^{(1)'}(\varsigma)/\omega'(\varsigma)\,|_{\varsigma\to\sqrt{m}} \tag{49}$$

or

$$K_1 = \frac{\sqrt{\pi c}}{R}\left(\sum_{k=-N}^{N}{}' k e^{k-1} a_k^{(1)}\right) \quad \text{with} \quad c = \sqrt{a^2-b^2}, \quad e = \sqrt{m} = \sqrt{(a-b)/(a+b)}. \tag{50}$$

3 Numerical examples for the infinite matrix case

Example 1 In the first example, the case for two phases is considered (Fig. 2). The elastic constants for the inclusion and the matrix are denoted by G_1, κ_1 and G_2, κ_2, respectively. $\kappa_1 = \kappa_2 = 1.8$ is assumed in the example. The inclusion has a shape of an ellipse with two half-axes "a" and "b." In addition, a crack $(-c, c)(c = \sqrt{a^2 - b^2})$ is embedded in the inclusion. The remote loading σ_y^∞ is applied at infinity. In computation, we truncate $N = 55$ terms in the Laurent series expansion for the complex potentials. Clearly, the general technique used for the case of three phases can easily be used for the present example.

Under the conditions (i) $b/a = 0.25, 0.5, 0.75$ and 0.9, (ii) $G_2/G_1 = 10, 2, 1, 0.5$ and 0.1, and (iii) the remote loading σ_y^∞, the stress intensity factors can be expressed as

$$K_1 = f_1(b/a, G_2/G_1)\sigma_y^\infty\sqrt{\pi c}, \ \left(\text{with} \quad c = \sqrt{a^2-b^2}\right). \tag{51}$$

The computed results for $f_1(b/a, G_2/G_1)$ are listed in Table 1.

It is seen from the plotted results that, in the case of $G_2/G_1 = 10$ or for a very weaker inclusion, the non-dimensional SIFs generally take the value less than unity. For example, we have $f_1\,|_{b/a=0.5\,G_2/G_1=10} = 0.1548$ and $f_1\,|_{b/a=0.5\,G_2/G_1=2} = 0.6130$. Since a weaker inclusion has a lower traction response under some deformation, this result is easy to see.

Table 1 Non-dimensional stress intensity factors $f_1(b/a, G_2/G_1)(= K_1/\sigma_y^\infty\sqrt{\pi c})$ [see Fig. 2 and Eq. (51)]

G_2/G_1 $b/a=$	10	2	1	0.5	0.1
0.25	0.1467	0.5992	1.0000	1.5682	3.9101
0.50	0.1548	0.6130	1.0000	1.5245	3.2993
0.75	0.1758	0.6497	1.0000	1.4052	2.2645
0.9	0.2099	0.7002	1.0000	1.2878	1.7240

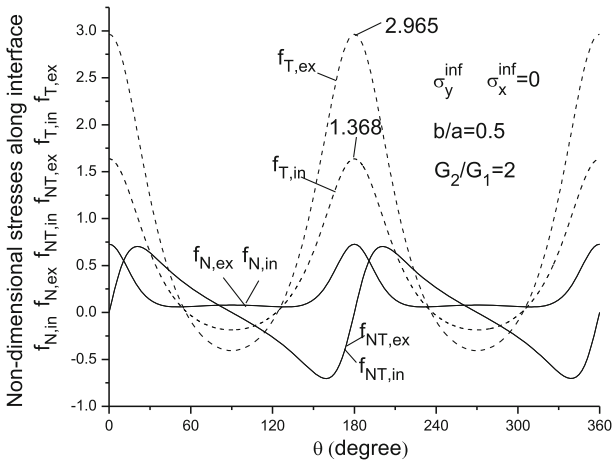

Fig. 3 Non-dimensional stresses $f_{N,\text{in}}(\theta)$, $f_{NT,\text{in}}(\theta)$, $f_{T,\text{in}}(\theta)$ (in the interior side of the interface), $f_{N,\text{ex}}(\theta)$, $f_{NT,\text{ex}}(\theta)$, $f_{T,\text{ex}}(\theta)$ (in the exterior side of the interface) in the case of (i) $b/a = 0.5$, (ii) remote loading σ_y^∞ and (iii) $G_2/G_1 = 2$ [see Fig. 2 and Eqs. (52), (53)]

On the contrary, in the case of $G_2/G_1 = 0.5$ or $G_2/G_1 = 0.1$, or for a very rigid inclusion, the non-dimensional SIFs generally take a value large than unity. For example, we have $f_1\,|_{b/a=0.5\,G_2/G_1=0.5} = 1.5245$ and $f_1\,|_{b/a=0.5\,G_2/G_1=0.1} = 3.2993$.

As stated previously, all the distributions of stresses can be found from the solution based on the suggested technique. In the case of $b/a = 0.5$ and the remote loading σ_y^∞, the computed results for σ_N, σ_{NT} and σ_T in the interior side of the interface, or from the inclusion side, are denoted by (Fig. 2)

$$\sigma_N = f_{N,\text{in}}(\theta)\sigma_y^\infty, \quad \sigma_{NT} = f_{NT,\text{in}}(\theta)\sigma_y^\infty, \quad \sigma_T = f_{T,\text{in}}(\theta)\sigma_y^\infty \quad (\text{at point } x = a\cos\theta,\ y = b\sin\theta). \tag{52}$$

Similarly, the computed results for σ_N, σ_{NT} and σ_T in the exterior side of the interface, or from the matrix side, are denoted by (Fig. 2)

$$\sigma_N = f_{N,\text{ex}}(\theta)\sigma_y^\infty, \quad \sigma_{NT} = f_{NT,\text{ex}}(\theta)\sigma_y^\infty, \quad \sigma_T = f_{T,\text{ex}}(\theta)\sigma_y^\infty. \\ (\text{at point } x = a\cos\theta,\ y = b\ \sin\theta) \tag{53}$$

For the case of (i) $b/a = 0.5$, (ii) remote loading σ_y^∞ and (iii) $G_2/G_1 = 2$, the computed results for non-dimensional stresses $f_{N,\text{in}}(\theta)$, $f_{NT,\text{in}}(\theta)$, $f_{T,\text{in}}(\theta)$, $f_{N,\text{ex}}(\theta)$, $f_{NT,\text{ex}}(\theta)$, $f_{T,\text{ex}}(\theta)$ are plotted in Fig. 3. Theoretically, there should be $f_{N,\text{in}}(\theta) = f_{N,\text{ex}}(\theta)$ and $f_{NT,\text{in}}(\theta) = f_{NT,\text{ex}}(\theta)$. From Fig. 3, we see that those curves are merged together. This will prove that an accurate result is achieved in the present technique. On the other hand, a significant difference can be found between the $f_{T,\text{in}}(\theta)$ and $f_{T,\text{ex}}(\theta)$. For example, from Fig. 3 we find $f_{T,\text{in}}(\theta)\,|_{\theta=180^\circ} = 1.368$, $f_{T,\text{ex}}(\theta)\,|_{\theta=180^\circ} = 2.965$ and $f_{T,\text{in}}(\theta)\,|_{\theta=180^\circ} < f_{T,\text{ex}}(\theta)\,|_{\theta=180^\circ}$.

Similarly, for the case of (i) $b/a = 0.5$, (ii) remote loading σ_y^∞ and (iii) $G_2/G_1 = 0.5$, the computed results for non-dimensional stresses $f_{N,\text{in}}(\theta)$, $f_{NT,\text{in}}(\theta)$, $f_{T,\text{in}}(\theta)$, $f_{N,\text{ex}}(\theta)$, $f_{NT,\text{ex}}(\theta)$, $f_{T,\text{ex}}(\theta)$ are plotted in Fig. 4. The same results in computation, or $f_{N,\text{in}}(\theta) = f_{N,\text{ex}}(\theta)$ and $f_{NT,\text{in}}(\theta) = f_{NT,\text{ex}}(\theta)$, can be found from Fig. 4. Contrary to the previous case, in this case we find $f_{T,\text{in}}(\theta)\,|_{\theta=180^\circ} = 1.690$, $f_{T,\text{ex}}(\theta)\,|_{\theta=180^\circ} = 1.094$ and $f_{T,\text{in}}(\theta)\,|_{\theta=180^\circ} > f_{T,\text{ex}(\theta)}\,|_{\theta=180^\circ}$.

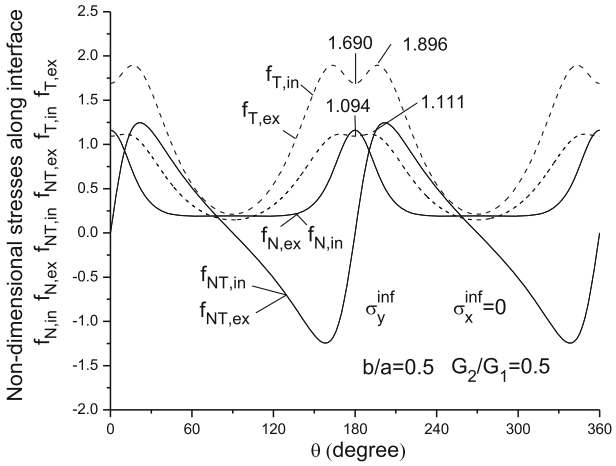

Fig. 4 Non-dimensional stresses $f_{N,\mathrm{in}}(\theta)$, $f_{NT,\mathrm{in}}(\theta)$, $f_{T,\mathrm{in}}(\theta)$ (in the interior side of the interface), $f_{N,\mathrm{ex}}(\theta)$, $f_{NT,\mathrm{ex}}(\theta)$, $f_{T,\mathrm{ex}}(\theta)$ (in the exterior side of the interface) in the case of (i) $b/a = 0.5$, (ii) remote loading σ_y^{∞} and (iii) $G_2/G_1 = 0.5$ [see Fig. 2 and Eqs. (52), (53)]

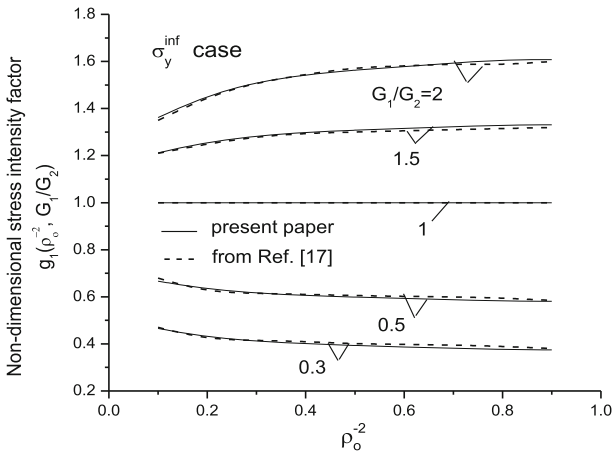

Fig. 5 Non-dimensional stress intensity factors $g_1(\rho_o^{-2}, G_1/G_2)$ [see Fig. 2 and Eq. (55)]

Example 2 In the second example, the case for two phases is considered (Fig. 2). In the example, the interface is the substitution of $\varsigma = \sqrt{m}\rho_o \exp(i\theta)(\rho_o > 1)$ in the mapping function $z = \omega(\varsigma) = R(\varsigma + m/\varsigma)$. In this case, we have the following two half-axes for the interface:

$$a_{\rho o} = \frac{c}{2}\left(\rho_o + \frac{1}{\rho_o}\right), \quad b_{\rho o} = \frac{c}{2}\left(\rho_o - \frac{1}{\rho_o}\right), \quad \frac{b_{\rho o}}{a_{\rho o}} = \frac{\rho_o^2 - 1}{\rho_o^2 + 1} \quad \text{with} \quad c = \sqrt{a^2 - b^2}. \tag{54}$$

From Eq. (54) we see that if $\rho_o \to \infty$, $b_{\rho o}/a_{\rho o} \to 1$ or the interface becomes a large circle. The elastic constants for the inclusion and the matrix are denoted by G_1, κ_1 and G_2, κ_2, respectively. $\kappa_1 = \kappa_2 = 2.2$ (to coincide with the value used in [17]) is assumed in the example.

Under the conditions (i) $\rho_o^{-2} = 0.1, 0.2, \ldots, 0.9$, (ii) $G_1/G_2 = 2$, 1.5,1, 0.5 and 0.3 and (iii) the remote loading σ_y^{∞}, the stress intensity factors can be expressed as

$$K_1 = g_1(\rho_o^{-2}, G_1/G_2)\sigma_y^{\infty}\sqrt{\pi c}, \quad \left(\text{with } c = \sqrt{a^2 - b^2}\right). \tag{55}$$

The computed results for $g_1(\rho_o^{-2}, G_1/G_2)$ are plotted in Fig 5. In addition, the previously obtained results in [17] are also plotted in Fig. 5.

From the plotted results, we see that the differences for the computed results from different sources of computation are minor. Those differences may come from the following factors. In the present study, the

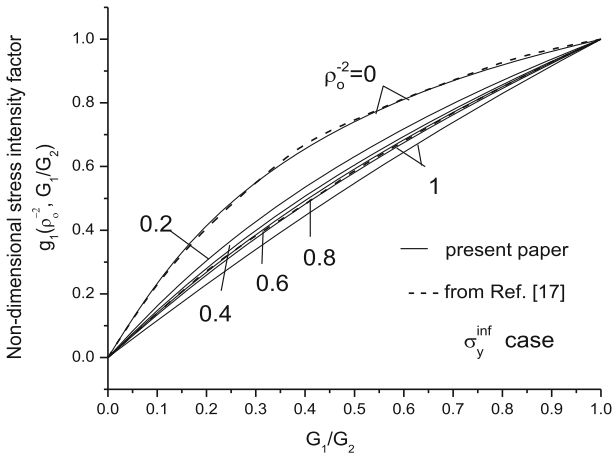

Fig. 6 Non-dimensional stress intensity factors $g_1(\rho_o^{-2}, G_1/G_2)$ [see Fig. 2 and Eq. (55)]

traction-free condition along the crack is satisfied in a weaker form. To this end, we can apply the following operator $\frac{1}{2\pi i}\int_{\Gamma_0}[\ldots]\varsigma^{j-1}\mathrm{d}\varsigma$ $(j = -N, -(N-1), \ldots, -2, -1, 1, 2, \ldots, N-1, N)$ to Eq. (14). In addition, in Ref. [17], the traction-free condition along the crack is satisfied along the crack face by expanding the complex potentials in Laurent series. Secondly, the terms truncated in two sources may not be the same.

Under the other conditions (i) $\rho_o^{-2} = 0, 0.1, 0.2, \ldots, 0.9, 1$, (ii) $G_1/G_2 = 0, 0.1, 0.2, \ldots, 1.0$ and (iii) the remote loading σ_y^∞, the stress intensity factors are still expressed by Eq. (55). The computed results for $g_1(\rho_o^{-2}, G_1/G_2)$ are plotted in Fig 6. In computation, the case for $\rho_o^{-2} = 0$ is approximated by $\rho_o^{-2} = 10^{-5}$. The result for $\rho_o^{-2} = 1$ is derived from the computed results for $\rho_o^{-2} = 0.9$ and $\rho_o^{-2} = 0.95$ and usage of an extrapolation. The case for $G_1/G_2 = 0$ is approximated by the case for $G_1/G_2 = 10^{-3}$. In addition, the previously obtained results in [17] are also plotted in Fig. 6.

From Fig. 6, we see that for the case of $\rho_o^{-2} \to 0$ or $\rho_o \to \infty$, the results from two sources are nearly the same. In addition, for the case of $\rho_o \to 1 (\rho_o > 1)$ some differences are found from different sources of computation. The reason for the difference has been explained previously.

Example 3 In the third example, the case for three phases is considered (Fig. 1). The elastic constants for the inclusion, the elliptic layer and the matrix are denoted by G_1, κ_1, G_2, κ_2 and G_3, κ_3, respectively. We choose $\kappa_1 = \kappa_2 = \kappa_3 = 1.8$. The inclusion has a shape of an ellipse with two half-axes "a" and "b." The elliptic layer is bound by two interfaces Σ_1 and Σ_2, which are the mappings of the circles Γ_1 (or $\varsigma = \rho_1 e^{i\theta} \in \Gamma_1$ with $\rho_1 = 1$) and Γ_2 (or $\varsigma = \rho_2 e^{i\theta} \in \Gamma_2$), respectively. In the example, $\rho_2 = 1.5$ is assumed.

The remote loading σ_y^∞ is applied at infinity. It is truncated at $N = 55$ terms in the Laurent series expansion for the complex potentials. Clearly, the general technique used for the case of three phases can easily be used in the present example.

In computation, we assume the following conditions: (i) $\rho_1 = 1$, $\rho_2 = 1.5$, (ii) $b/a = 0.25, 0.5, 0.75, 0.9$ and (iii) $G_3/G_1 = \beta$, 10, 2, 1, 0.5 and 0.1, $G_2/G_1 = \sqrt{\beta} = \sqrt{10} = 3.162$, $\sqrt{2} = 1.414$, 1, $\sqrt{0.5} = 0.7073$ and $\sqrt{0.1} = 0.316$, respectively.

The computed stress intensity factors can be expressed as

$$K_1 = f_2(b/a, G_3/G_1)\sigma_y^\infty\sqrt{\pi c} \quad \text{with } G_2/G_1 = \sqrt{G_3/G_1}. \tag{56}$$

The computed results for $f_2(b/a, G_3/G_1)$ are listed in Table 2.

As stated previously, all the distributions of stresses can be found from the suggested technique. In the case of $b/a = 0.5$ and remote loading σ_y^∞, the computed results for σ_N, σ_{NT} and σ_T in the interior side and the exterior side of the first interface Σ_1 $(z = \omega(\varsigma) \in \Sigma_1, \varsigma = e^{i\theta} \in \Gamma_1)$ are denoted by

$$\sigma_N = f_{N,\mathrm{in1}}(\theta)\sigma_y^\infty, \quad \sigma_{NT} = f_{NT,\mathrm{in1}}(\theta)\sigma_y^\infty, \quad \sigma_T = f_{T,\mathrm{in1}}(\theta)\sigma_y^\infty$$
$$(\text{at point } x = a\cos\theta,\ y = b\sin\theta \text{ in the interior side of the first interface } \Sigma_1), \tag{57}$$
$$\sigma_N = f_{N,\mathrm{ex1}}(\theta)\sigma_y^\infty, \quad \sigma_{NT} = f_{NT,\mathrm{ex1}}(\theta)\sigma_y^\infty, \quad \sigma_T = f_{T,\mathrm{ex1}}(\theta)\sigma_y^\infty$$
$$(\text{at point } x = a\cos\theta,\ y = b\sin\theta, \text{ in the exterior side of the first interface } \Sigma_1). \tag{58}$$

Table 2 Non-dimensional stress intensity factors $f_2(b/a, G_3/G_1)(= K_1/\sigma_y^{\infty}\sqrt{\pi c})$ with $G_2/G_1 = \sqrt{G_3/G_1}$ [see Fig. 1 and Eq. (56)]

G_3/G_1 $b/a =$	10	2	1	0.5	0.1
0.25	0.1746	0.6187	1.0000	1.5500	3.6793
0.50	0.1844	0.6376	1.0000	1.4792	2.9301
0.75	0.2092	0.6770	1.0000	1.3641	2.1312
0.9	0.2453	0.7212	1.0000	1.2714	1.7056

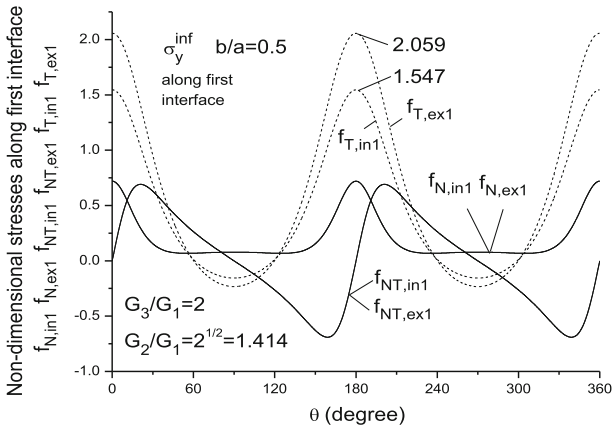

Fig. 7 Non-dimensional stresses $f_{N,\mathrm{in1}}(\theta)$, $f_{NT,\mathrm{in1}}(\theta)$, $f_{T,\mathrm{in1}}(\theta)$ (in the interior side of interface Σ_1), $f_{N,\mathrm{ex1}}(\theta)$, $f_{NT,\mathrm{ex1}}(\theta)$, $f_{T,\mathrm{ex1}}(\theta)$ (in the exterior side of interface Σ_1) in the case of (1) $b/a = 0.5$, (2) remote loading σ_y^{∞} and (3) $G_2/G_1 = \sqrt{2} = 1.414$, $G_3/G_1 = 2$ [see Fig. 1 and Eqs. (57), (58)]

Similarly, the computed results for σ_N, σ_{NT} and σ_T in the interior side and the exterior side of the second interface Σ_2 ($z = \omega(\varsigma) \in \Sigma_2$, $\varsigma = \rho_2 e^{i\theta} \in \Gamma_2$ with $\rho_2 = 1.5$), are denoted by

$$\begin{aligned}\sigma_N &= f_{N,\mathrm{in2}}(\theta)\sigma_y^{\infty}, \quad \sigma_{NT} = f_{NT,\mathrm{in2}}(\theta)\sigma_y^{\infty}, \quad \sigma_T = f_{T,\mathrm{in2}}(\theta)\sigma_y^{\infty} \\ &\quad (\text{at point } x = R(\rho_2 + m/\rho_2)\cos\theta,\ y = R(\rho_2 - m/\rho_2)\sin\theta \\ &\quad \text{in the interior side of the second interface } \Sigma_2), \qquad (59) \\ \sigma_N &= f_{N,\mathrm{ex2}}(\theta)\sigma_y^{\infty}, \quad \sigma_{NT} = f_{NT,\mathrm{ex2}}(\theta)\sigma_y^{\infty}, \quad \sigma_T = f_{T,\mathrm{ex2}}(\theta)\sigma_y^{\infty} \\ &\quad (\text{at point } x = R(\rho_2 + m/\rho_2)\cos\theta,\ y = R(\rho_2 - m/\rho_2)\sin\theta \\ &\quad \text{in the exterior side of the second interface } \Sigma_2). \qquad (60)\end{aligned}$$

In the first group of computation, assuming $b/a = 0.5$, $G_2/G_1 = \sqrt{\beta}$, $G_3/G_1 = \beta$ with $\sqrt{\beta} = 1.414$, $\beta = 2$, the computed results for non-dimensional stresses $f_{N,\mathrm{in1}}(\theta)$, $f_{NT,\mathrm{in1}}(\theta)$, $f_{T,\mathrm{in1}}(\theta)$ and $f_{N,\mathrm{ex1}}(\theta)$, $f_{NT,\mathrm{ex1}}(\theta)$, $f_{T,\mathrm{ex1}}(\theta)$ along the interface Σ_1 are plotted in Fig. 7. From Fig. 7, we see that $f_{N,\mathrm{in1}}(\theta) = f_{N,\mathrm{ex1}}(\theta)$, $f_{NT,\mathrm{in1}}(\theta) = f_{NT,\mathrm{ex1}}(\theta)$. That is to say, the continuity conditions for the stress components σ_N and σ_{NT} along the interface are satisfied with higher accuracy in the numerical example. In addition, we find that $f_{T,\mathrm{in1}}(\theta) \neq f_{T,\mathrm{ex1}}(\theta)$. For example, $f_{T,\mathrm{in1}}(\theta)\,|_{\theta=180^\circ} = 1.547$, $f_{T,\mathrm{ex1}}(\theta)\,|_{\theta=180^\circ} = 2.059$, and $f_{T,\mathrm{in1}}(\theta)\,|_{\theta=180^\circ} < f_{T,\mathrm{ex1}}(\theta)\,|_{\theta=180^\circ}$.

Under the same condition $G_2/G_1 = \sqrt{\beta}$, $G_3/G_1 = \beta$with $\beta = 2$, the computed results for non-dimensional stresses $f_{N,\mathrm{in2}}(\theta)$, $f_{NT,\mathrm{in2}}(\theta)$, $f_{T,\mathrm{in2}}(\theta)$ and $f_{N,\mathrm{ex2}}(\theta)$, $f_{NT,\mathrm{ex2}}(\theta)$, $f_{T,\mathrm{ex2}}(\theta)$ along the interface Σ_2 are plotted in Fig. 8. In addition, we still find that $f_{T,\mathrm{in2}}(\theta) \neq f_{T,\mathrm{ex2}}(\theta)$. For example, $f_{T,\mathrm{in2}}(\theta)\,|_{\theta=180^\circ} = 1.293$, $f_{T,\mathrm{ex2}}(\theta)\,|_{\theta=180^\circ}$. $= 1.763$, and $f_{T,\mathrm{in2}}(\theta)\,|_{\theta=180^\circ} < f_{T,\mathrm{ex2}}(\theta)\,|_{\theta=180^\circ}$.

In the second group of computation, assuming $b/a = 0.5$, $G_2/G_1 = \sqrt{\beta}$, $G_3/G_1 = \beta$ with $\sqrt{\beta} = 0.707$, $\beta = 0.5$, the computed results for non-dimensional stresses $f_{N,\mathrm{in1}}(\theta)$, $f_{NT,\mathrm{in1}}(\theta)$, $f_{T,\mathrm{in1}}(\theta)$ and $f_{N,\mathrm{ex1}}(\theta)$, $f_{NT,\mathrm{ex1}}(\theta)$, $f_{T,\mathrm{ex1}}(\theta)$ along the interface Σ_1 are plotted in Fig. 9. From the plotted results, we see that $f_{N,\mathrm{in1}}(\theta) = f_{N,\mathrm{ex1}}(\theta)$, $f_{NT,\mathrm{in1}}(\theta) = f_{NT,\mathrm{ex1}}(\theta)$. That is to say, the continuity conditions for the stress components σ_N and σ_{NT} along the interface are satisfied with higher accuracy. In addition, we find that $f_{T,\mathrm{in1}}(\theta) \neq f_{T,\mathrm{ex1}}(\theta)$. For example, $f_{T,\mathrm{in1}}(\theta)\,|_{\theta=180^\circ} = 2.241$, $f_{T,\mathrm{ex1}}(\theta)\,|_{\theta=180^\circ} = 1.745$, and

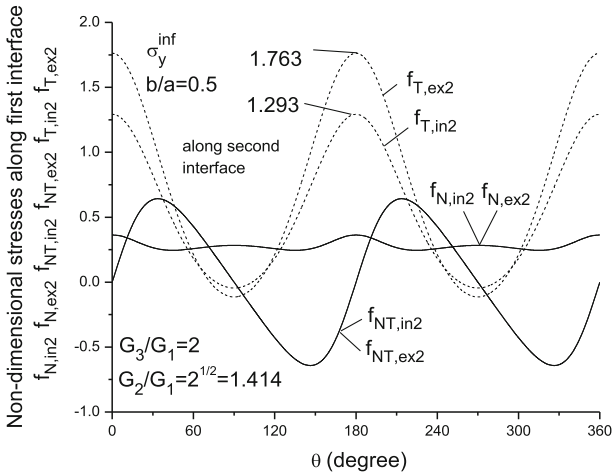

Fig. 8 Non-dimensional stresses $f_{N,\text{in}2}(\theta)$, $f_{NT,\text{in}2}(\theta)$, $f_{T,\text{in}2}(\theta)$ (in the interior side of interface Σ_2), $f_{N,\text{ex}2}(\theta)$, $f_{NT,\text{ex}2}(\theta)$, $f_{T,\text{ex}2}(\theta)$ (in the exterior side of interface Σ_2) in the case of (1) $b/a = 0.5$, (2) remote loading σ_y^{∞} and (3) $G_2/G_1 = \sqrt{2} = 1.414$, $G_3/G_1 = 2$ [see Fig. 1 and Eqs. (59), (60)]

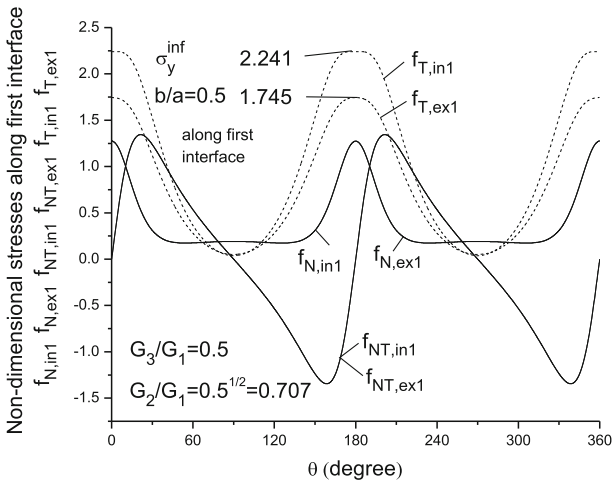

Fig. 9 Non-dimensional stresses $f_{N,\text{in}1}(\theta)$, $f_{NT,\text{in}1}(\theta)$, $f_{T,\text{in}1}(\theta)$ (in the interior side of interface Σ_1), $f_{N,\text{ex}1}(\theta)$, $f_{NT,\text{ex}1}(\theta)$, $f_{T,\text{ex}1}(\theta)$ (in the exterior side of interface Σ_1) in the case of (1) $b/a = 0.5$, (2) remote loading σ_y^{∞} and (3) $G_2/G_1 = \sqrt{0.5} = 0.707$, $G_3/G_1 = 0.5$ [see Fig. 1 and Eqs. (57), (58)]

$f_{T,\text{in}1}(\theta)\,|_{\theta=180^\circ} > f_{T,\text{ex}1}(\theta)\,|_{\theta=180^\circ}$. This result, or $f_{T,\text{in}1}(\theta)\,|_{\theta=180^\circ} > f_{T,\text{ex}1}(\theta)\,|_{\theta=180^\circ}$ (in the case of $\beta = 0.5$), is different from the result in the first group, where $f_{T,\text{in}1}(\theta)\,|_{\theta=180^\circ} < f_{T,\text{ex}1}(\theta)\,|_{\theta=180^\circ}$ (in the case of $\beta = 2$).

Similarly, under the same condition the computed results for non-dimensional stresses $f_{N,\text{in}2}(\theta)$, $f_{NT,\text{in}2}(\theta)$, $f_{T,\text{in}2}(\theta)$ and $f_{N,\text{ex}2}(\theta)$, $f_{NT,\text{ex}2}(\theta)$, $f_{T,\text{ex}2}(\theta)$ along the interface Σ_2 are plotted in Fig. 10. In addition, we still find that $f_{T,\text{in}2}(\theta) \neq f_{T,\text{ex}2}(\theta)$. For example, $f_{T,\text{in}2}(\theta)\,|_{\theta=180^\circ} = 1.312$, $f_{T,\text{ex}2}(\theta)\,|_{\theta=180^\circ} . = 0.965$, and $f_{T,\text{in}2}(\theta)\,|_{\theta=180^\circ} > f_{T,\text{ex}2}(\theta)\,|_{\theta=180^\circ}$.

4 A crack embedded in multiple elliptic layers with different elastic properties for the exterior finite elliptic matrix case

The problem for a crack embedded in multiple elliptic layers with different elastic properties for the exterior finite elliptic matrix case is studied below (Fig. 11). This topic is first investigated in this paper.

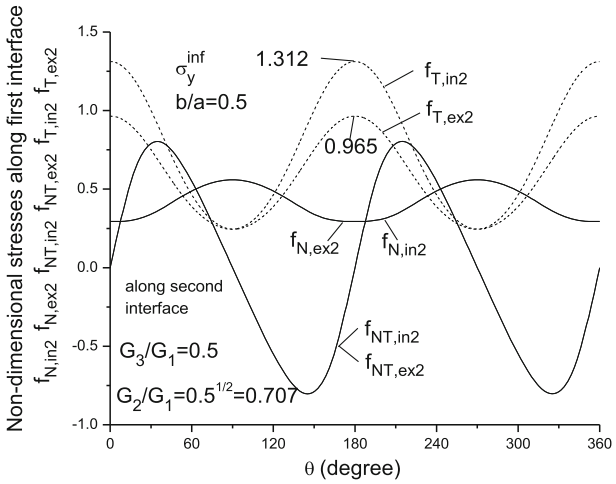

Fig. 10 Non-dimensional stresses $f_{N,\text{in}2}(\theta)$, $f_{NT,\text{in}2}(\theta)$, $f_{T,\text{in}2}(\theta)$ (in the interior side of interface Σ_2), $f_{N,\text{ex}2}(\theta)$, $f_{NT,\text{ex}2}(\theta)$, $f_{T,\text{ex}2}(\theta)$ (in the exterior side of interface Σ_2) in the case of (i) $b/a = 0.5$, (ii) remote loading σ_y^{∞} and (iii) $G_2/G_1 = \sqrt{0.5} = 0.707$, $G_3/G_1 = 0.5$ [see Fig. 1 and Eqs. (59), (60)]

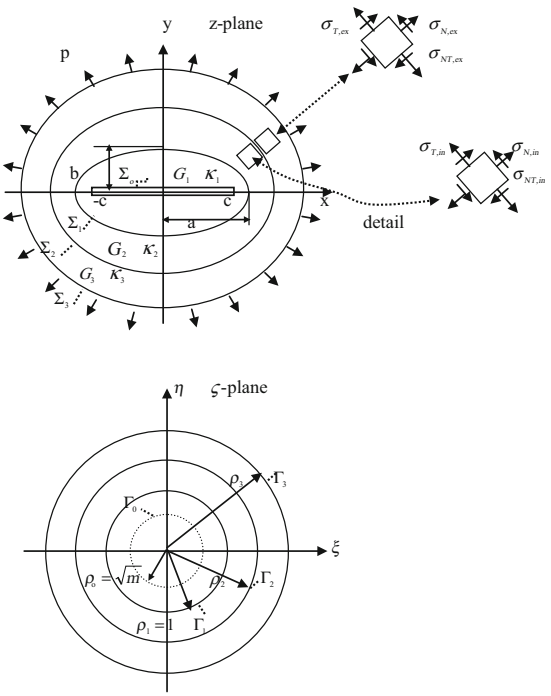

Fig. 11 Mapping relations: (a) the finite elliptic inclusion with two half-axes "a" and "b" with a crack $(-c, c)$ $c = \sqrt{a^2 - b^2}$ (in the z-plane) and elastic constants G_1, κ_1 mapped into ring region $\sqrt{m} < |\varsigma| \le 1$ (in the ς-plane with $m = (a-b)/(a+b)$), (b) the elliptic layer bound by two interfaces Σ_1 and Σ_2 (in the z-plane) with elastic constants G_2, κ_2 mapped into ring region bound by two circles Γ_1 and Γ_2, or $\rho_1 \le |\varsigma| \le \rho_2$ with $\rho_1 = 1$ (in the ς-plane), (c) the elliptic layer bound by two interfaces Σ_2 and Σ_3 (in the z-plane) with elastic constants G_3, κ_3 mapped into ring region bound by two circles Γ_2 and Γ_3, or $\rho_2 \le |\varsigma| \le \rho_3$ (in the ς-plane)

4.1 Analysis for the exterior finite elliptic matrix case

For the exterior finite elliptic matrix case, the whole region is composed of three-phase composites: (i) the elliptic inclusion with the elastic constants G_1, κ_1. In addition, a crack $(-cc)$ with $c = \sqrt{a^2 - b^2}$ is embedded in the inclusion. (ii) The elliptic layer bound by two interfaces Σ_1 and Σ_2 with the elastic constants G_2, κ_2,

and (iii) the elliptic layer bound by two interfaces Σ_2 and Σ_3 with the elastic constants G_3, κ_3. In addition, the normal traction "p" is applied along the boundary Σ_3 (Fig. 11).

Clearly, since only the boundary condition at the exterior layer in this paper has a difference with respect to that studied in the Sect. 2, Eqs. (1) to (27) and (32) to (45) are still useful in the present case.

However, the condition at the exterior layer is quite different from that in Sect. 2. In Sect. 2, or in the infinite matrix case, for the vector $\{A_3\}_{4N}$ we have the following property: $a_1^{(3)} = h_1 R$, $a_k^{(3)} = 0$ (for $k \geq 2$), $b_1^{(3)} = h_2 R$, $b_k^{(3)} = 0$ (for $k \geq 2$). In addition, for the finite matrix case, the vector $\{A_3\}_{4N}$ must satisfy the traction boundary condition addressed below or Eq. (61).

Now we consider the boundary value condition along the boundary Σ_3 (Fig. 11). In the present study, a normal traction "p" is applied along the boundary Σ_3. On the mapping plane, the condition can be expressed as

$$\phi^{(3)}(\varsigma) + \frac{\omega(\varsigma)}{\overline{\omega'(\varsigma)}}\overline{\phi'^{(3)}(\varsigma)} + \overline{\psi^{(3)}(\varsigma)} = p\omega(\varsigma) = pR(\varsigma + \frac{m}{\varsigma}), \quad (\varsigma \in \Gamma_3). \tag{61}$$

After applying the following operator $\frac{1}{2\pi i}\int_{\Gamma_3}\{\ldots\}\varsigma^{j-1}\mathrm{d}\varsigma$, $(j = -N, -(N-1), \ldots, -2, -1, 1, 2, \ldots, N-1, N)$ to both sides of Eq. (61), we have the following algebraic equation:

$$[\mathbf{U}]_{2\mathbf{N}\times 4\mathbf{N}}\{A_3\}_{4N} = \{q\}_{2N} \tag{62}$$

where the matrix $[\mathbf{U}]_{2\mathbf{N}\times 4\mathbf{N}}$ can be evaluated by the technique used previously. In addition, the vector $\{q\}_{2N}$ can be expressed as

$$\begin{aligned}\{q\}_{2N} &= \{0\ 0\ldots 0\ldots pR\ mpR\ 0\ldots 0\ 0\}^{\mathrm{T}}\\ &(\text{or } q_N = pR,\ q_{N+1} = mpR,\ q_k\ |_{k\neq N\ or\quad k\neq N+1} = 0).\end{aligned} \tag{63}$$

Substituting Eq. (43) in (62), we will find

$$[\mathbf{U}_{31}]_{2\mathbf{N}\times 2\mathbf{N}}\{A_{1p}\}_{2N} = \{q\}_{2N} \tag{64}$$

where

$$[\mathbf{U}_{31}]_{2\mathbf{N}\times 2\mathbf{N}} = [\mathbf{U}]_{2\mathbf{N}\times 4\mathbf{N}}[\mathbf{T}_{31}]_{4\mathbf{N}\times 2\mathbf{N}}. \tag{65}$$

Finally, from Eq. (64) we can get a solution for the vector $\{A_{1p}\}_{2N}$. In addition, from the obtained vector $\{A_{1p}\}_{2N}$, we can obtain three vectors $\{A_1\}_{2N}$, $\{A_2\}_{2N}$ and $\{A_3\}_{2N}$ by using Eqs. (21), (42) and (43), respectively. Alternatively speaking, the boundary value problem is finally solved.

4.2 Numerical example for the exterior finite elliptic matrix case

In the example, the case for three phases is considered (Fig. 11). The elastic constants for the inclusion and the two elliptic layers are denoted by G_1, κ_1, G_2, κ_2 and G_3, κ_3, respectively. We choose $\kappa_1 = \kappa_2 = \kappa_3 = 1.8$. The inclusion has a shape of an ellipse with two half-axes "a" and "b." The crack $(-c, c)$ with $c = \sqrt{a^2 - b^2}$ is embedded in the inclusion. The first elliptic layer is bound by two interfaces Σ_1 and Σ_2, which are the mappings of the circles Γ_1 (or $\varsigma = \rho_1 e^{i\theta} \in \Gamma_1$ with $\rho_1 = 1$) and Γ_2(or $\varsigma = \rho_2 e^{i\theta} \in \Gamma_2$), respectively. In the example, $\rho_2 = 1.5$ is assumed. The second elliptic layer is bound by the interfaces Σ_2 and the boundary Σ_3, which are the mappings of the circles Γ_2(or $\varsigma = \rho_2 e^{i\theta} \in \Gamma_2$) and Γ_3(or $\varsigma = \rho_3 e^{i\theta} \in \Gamma_2$), respectively. In the example, $\rho_3 = 2$ is assumed (Fig. 11).

Along the exterior boundary Σ_3, the loading $\sigma_N = p$ is applied. It is truncated at $N = 55$ terms in the Laurent series expansion for the complex potentials.

In the computation, we assume the following conditions: (i) $\rho_0 = \sqrt{m}$, $\rho_1 = 1$, $\rho_2 = 1.5$ and $\rho_3 = 2$, (ii) $b/a = 0.25, 0.5, 0.75, 0.9$, and (iii) $G_3/G_1 = \beta = 10, 2, 1, 0.5$ and 0.1, $G_2/G_1 = \sqrt{\beta} = \sqrt{10} = 3.162$, $\sqrt{2} = 1.414$, 1, $\sqrt{0.5} = 0.7073$ and $\sqrt{0.1} = 0.316$, respectively.

The computed stress intensity factors can be expressed as

$$K_1 = g(b/a, G_3/G_1)p\sqrt{\pi c} \quad \text{with } G_2/G_1 = \sqrt{G_3/G_1} \quad c = \sqrt{a^2 - b^2}. \tag{66}$$

Table 3 Non-dimensional stress intensity factors $g(b/a, G_3/G_1)(= K_1/p\sqrt{\pi c})$ with $G_2/G_1 = \sqrt{G_3/G_1}$ [see Fig. 11 and Eq. (66)]

G_3/G_1 $b/a=$	10	2	1	0.5	0.1
0.25	0.6123	1.5352	2.1604	2.9431	5.4091
0.5	0.4797	1.1578	1.5680	2.0329	3.2295
0.75	0.4302	0.9609	1.2254	1.4842	2.0005
0.9	0.4431	0.8939	1.0804	1.2420	1.5109

The computed results for $g(b/a, G_3/G_1)$ are listed in Table 3.

It is seen from the plotted results that, in the case of $G_2/G_1 = 10$ or for a very weak inclusion, the non-dimensional SIFs (stress intensity factors) generally take a value smaller than their counterparts in the case of $G_2/G_1 = 1$. For example, we have $g\,|_{b/a=0.5\,G_2/G_1=10} = 0.4797$ and $g\,|_{b/a=0.5\,G_2/G_1=2} = 1.1578$ and $g\,|_{b/a=0.5\,G_2/G_1=1} = 1.5680$. Since a weaker inclusion has a lower traction response under some deformation, this result is easy to see.

On the contrary, it is seen from the plotted results that, in the case of $G_2/G_1 = 0.1$ or for a very rigid inclusion, the non-dimensional SIFs generally take a value larger than their counterparts in the case of $G_2/G_1 = 1$. For example, we have $g\,|_{b/a=0.5\,G_2/G_1=0.1} = 3.2295$ and $g\,|_{b/a=0.5\,G_2/G_1=0.5} = 2.0329$ and $g\,|_{b/a=0.5\,G_2/G_1=1} = 1.5680$. Since a rigid inclusion has a higher traction response under some deformation, this result is easy to see.

As stated previously, all the distributions of stresses can be found from the suggested technique. In the case of $b/a = 0.5$ and loading $\sigma_N = p$ along Σ_3 (Fig. 11), the computed results for σ_N, σ_{NT} and σ_T in the interior side and the exterior side of the first interface Σ_1 ($z = \omega(\varsigma) \in \Sigma_1$, $\varsigma = e^{i\theta} \in \Gamma_1$) are denoted by

$$\sigma_N = f_{N,\text{in1}}(\theta)p, \quad \sigma_{NT} = f_{NT,\text{in1}}(\theta)p, \quad \sigma_T = f_{T,\text{in1}}(\theta)p$$
$$\text{(at point } x = a\cos\theta,\ y = b\sin\theta \text{ in the interior side of the first interface } \Sigma_1), \tag{67}$$
$$\sigma_N = f_{N,\text{ex1}}(\theta)p, \quad \sigma_{NT} = f_{NT,\text{ex1}}(\theta)p, \quad \sigma_T = f_{T,\text{ex1}}(\theta)p$$
$$\text{(at point } x = a\cos\theta,\ y = b\sin\theta, \text{ in the exterior side of the first interface } \Sigma_1). \tag{68}$$

Similarly, the computed results for σ_N, σ_{NT} and σ_T in the interior side and the exterior side of the second interface Σ_2 ($z = \omega(\varsigma) \in \Sigma_2$, $\varsigma = \rho_2 e^{i\theta} \in \Gamma_2$ with $\rho_2 = 1.5$), are denoted by

$$\sigma_N = f_{N,\text{in2}}(\theta)p, \quad \sigma_{NT} = f_{NT,\text{in2}}(\theta)p, \quad \sigma_T = f_{T,\text{in2}}(\theta)p$$
$$\text{(at point } x = R(\rho_2 + m/\rho_2)\cos\theta,\ y = R(\rho_2 - m/\rho_2)\sin\theta$$
$$\text{in the interior side of the second interface } \Sigma_2), \tag{69}$$
$$\sigma_N = f_{N,\text{ex2}}(\theta)p, \quad \sigma_{NT} = f_{NT,\text{ex2}}(\theta)p, \quad \sigma_T = f_{T,\text{ex2}}(\theta)p$$
$$\text{(at point } x = R(\rho_2 + m/\rho_2)\cos\theta,\ y = R(\rho_2 - m/\rho_2)\sin\theta$$
$$\text{in the exterior side of the second interface } \Sigma_2). \tag{70}$$

In the first group of computations, assuming $b/a = 0.5$, $G_2/G_1 = \sqrt{\beta}$, $G_3/G_1 = \beta$ with $\sqrt{\beta} = 1.414$, $\beta = 2$, the computed results for the non-dimensional stresses $f_{N,\text{in1}}(\theta)$, $f_{NT,\text{in1}}(\theta)$, $f_{T,\text{in1}}(\theta)$ and $f_{N,\text{ex1}}(\theta)$, $f_{NT,\text{ex1}}(\theta)$, $f_{T,\text{ex1}}(\theta)$ along the interface Σ_1 are plotted in Fig. 12. From Fig. 12, we see that $f_{N,\text{in1}}(\theta) = f_{N,\text{ex1}}(\theta)$, $f_{NT,\text{in1}}(\theta) = f_{NT,\text{ex1}}(\theta)$. That is to say, the continuity conditions for the stress components σ_N and σ_{NT} along the interface are satisfied with higher accuracy in the numerical example. In addition, we find that $f_{T,\text{in1}}(\theta) \neq f_{T,\text{ex1}}(\theta)$. For example, $f_{T,\text{in1}}(\theta)\,|_{\theta=180^\circ} = 2.585$, $f_{T,\text{ex1}}(\theta)\,|_{\theta=180^\circ} = 3.315$, and $f_{T,\text{in1}}(\theta)\,|_{\theta=180^\circ} < f_{T,\text{ex1}}(\theta)\,|_{\theta=180^\circ}$.

Under the same condition $G_2/G_1 = \sqrt{\beta}$, $G_3/G_1 = \beta$ with $\beta = 2$, the computed results for the non-dimensional stresses $f_{N,\text{in2}}(\theta)$, $f_{NT,\text{in2}}(\theta)$, $f_{T,\text{in2}}(\theta)$ and $f_{N,\text{ex2}}(\theta)$, $f_{NT,\text{ex2}}(\theta)$, $f_{T,\text{ex2}}(\theta)$ along the interface Σ_2 are plotted in Fig. 13. In addition, we still find that $f_{T,\text{in2}}(\theta) \neq f_{T,\text{ex2}}(\theta)$. For example, $f_{T,\text{in2}}(\theta)\,|_{\theta=180^\circ} = 1.574$, $f_{T,\text{ex2}}(\theta)\,|_{\theta=180^\circ}$. $= 2.010$, and $f_{T,\text{in2}}(\theta)\,|_{\theta=180^\circ} < f_{T,\text{ex2}}(\theta)\,|_{\theta=180^\circ}$.

In the second group of computation, assuming $b/a = 0.5$, $G_2/G_1 = \sqrt{\beta}$, $G_3/G_1 = \beta$with $\sqrt{\beta} = 0.707$, $\beta = 0.5$, the computed results for non-dimensional stresses $f_{N,\text{in1}}(\theta)$,$f_{NT,\text{in1}}(\theta)$, $f_{T,\text{in1}}(\theta)$ and $f_{N,\text{ex1}}(\theta)$,$f_{NT,\text{ex1}}(\theta)$, $f_{T,\text{ex1}}(\theta)$ along the interface Σ_1 are plotted in Fig. 14. From the plotted results, we see that $f_{N,\text{in1}}(\theta) = f_{N,\text{ex1}}(\theta)$, $f_{NT,\text{in1}}(\theta) = f_{NT,\text{ex1}}(\theta)$. That is to say, the continuity conditions for the stress components σ_N and σ_{NT} along the interface are satisfied with higher accuracy. In addition, we

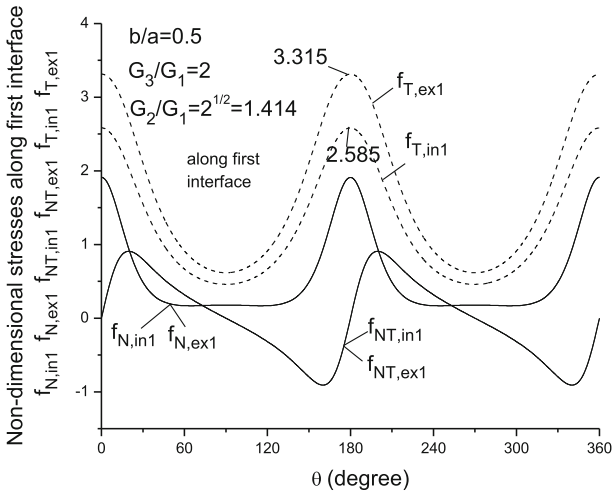

Fig. 12 Non-dimensional stresses $f_{N,\mathrm{in1}}(\theta)$, $f_{NT,\mathrm{in1}}(\theta)$, $f_{T,\mathrm{in1}}(\theta)$ (in the interior side of the interface Σ_1), $f_{N,\mathrm{ex1}}(\theta)$, $f_{NT,\mathrm{ex1}}(\theta)$, $f_{T,\mathrm{ex1}}(\theta)$ (in the exterior side of the interface Σ_1) in the case of (i) $b/a = 0.5$, (ii) boundary loading $\sigma_N = p$ and (iii) $G_2/G_1 = \sqrt{2}$=1.414, $G_3/G_1 = 2$ [see Fig. 11 and Eqs. (67), (68)]

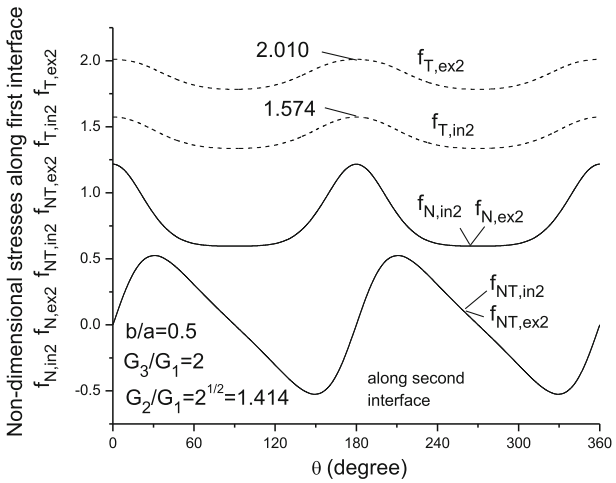

Fig. 13 Non-dimensional stresses $f_{N,\mathrm{in2}}(\theta)$, $f_{NT,\mathrm{in2}}(\theta)$, $f_{T,\mathrm{in2}}(\theta)$ (in the interior side of interface Σ_2), $f_{N,\mathrm{ex2}}(\theta)$, $f_{NT,\mathrm{ex2}}(\theta)$, $f_{T,\mathrm{ex2}}(\theta)$ (in the exterior side of interface Σ_2) in the case of (1) $b/a = 0.5$, (2) boundary loading $\sigma_N = p$ and (3) $G_2/G_1 = \sqrt{2} = 1.414$, $G_3/G_1 = 2$ [see Fig. 11 and Eqs. (69), (70)]

find that $f_{T,\mathrm{in1}}(\theta) \neq f_{T,\mathrm{ex1}}(\theta)$. For example, $f_{T,\mathrm{in1}}(\theta)\,|_{\theta=180^\circ} = 2.733$, $f_{T,\mathrm{ex1}}(\theta)\,|_{\theta=180^\circ} = 2.287$, and $f_{T,\mathrm{in1}}(\theta)\,|_{\theta=180^\circ} > f_{T,\mathrm{ex1}}(\theta)\,|_{\theta=180^\circ}$. This result, or $f_{T,\mathrm{in1}}(\theta)\,|_{\theta=180^\circ} > f_{T,\mathrm{ex1}}(\theta)\,|_{\theta=180^\circ}$ (in the case of $\beta = 0.5$), is different from the result in the first group, where $f_{T,\mathrm{in1}}(\theta)\,|_{\theta=180^\circ} < f_{T,\mathrm{ex1}}(\theta)\,|_{\theta=180^\circ}$ (in the case of $\beta = 2$).

Similarly, under the same condition the computed results for non-dimensional stresses $f_{N,\mathrm{in2}}(\theta)$, $f_{NT,\mathrm{in2}}(\theta)$, $f_{T,\mathrm{in2}}(\theta)$ and $f_{N,\mathrm{ex2}}(\theta)$, $f_{NT,\mathrm{ex2}}(\theta)$, $f_{T,\mathrm{ex2}}(\theta)$ along the interface Σ_2 are plotted in Fig. 15. In addition, we still find the result $f_{T,\mathrm{in2}}(\theta)\,|_{\theta=180^\circ} > f_{T,\mathrm{ex2}}(\theta)\,|_{\theta=180^\circ}$. In addition, we find $f_{T,\mathrm{in2}}(\theta)\,|_{\theta=90^\circ\ \max} = 1.787$, $f_{T,\mathrm{ex2}}(\theta)\,|_{\theta=90^\circ\ \max} = 1.363$.

5 Conclusions

The continuity conditions for traction and displacement have been introduced in Eqs. (32) and (33). In addition, those conditions were reduced in the following weaker form:

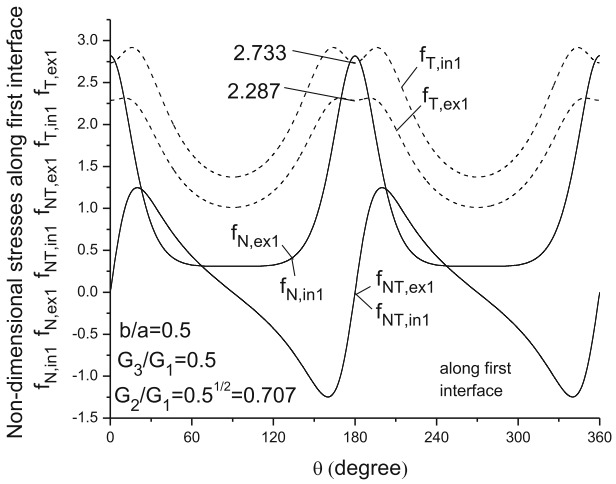

Fig. 14 Non-dimensional stresses $f_{N,\mathrm{in1}}(\theta)$, $f_{NT,\mathrm{in1}}(\theta)$, $f_{T,\mathrm{in1}}(\theta)$ (in the interior side of interface Σ_1), $f_{N,\mathrm{ex1}}(\theta)$, $f_{NT,\mathrm{ex1}}(\theta)$, $f_{T,\mathrm{ex1}}(\theta)$ (in the exterior side of interface Σ_1) in the case of (i) $b/a = 0.5$, (ii) boundary loading $\sigma_N = p$ and (iii) $G_2/G_1 = \sqrt{0.5} = 0.707$, $G_3/G_1 = 0.5$ [see Fig. 11 and Eqs. (67), (68)]

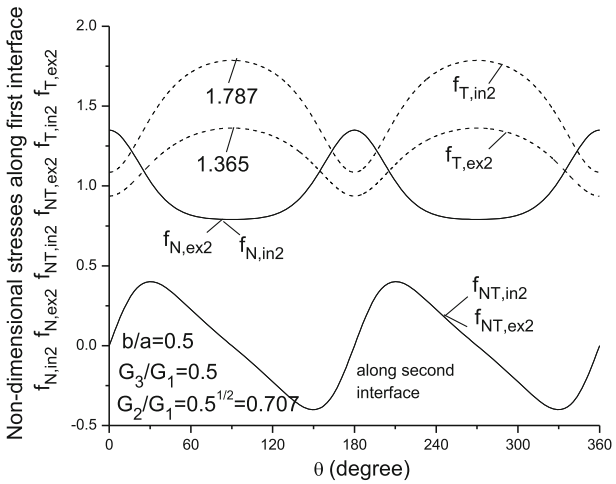

Fig. 15 Non-dimensional stresses $f_{N,\mathrm{in2}}(\theta)$, $f_{NT,\mathrm{in2}}(\theta)$, $f_{T,\mathrm{in2}}(\theta)$ (in the interior side of interface Σ_2), $f_{N,\mathrm{ex2}}(\theta)$, $f_{NT,\mathrm{ex2}}(\theta)$, $f_{T,\mathrm{ex2}}(\theta)$ (in the exterior side of interface Σ_2) in the case of (i) $b/a = 0.5$, (ii) boundary loading $\sigma_N = p$ and (iii) $G_2/G_1 = \sqrt{0.5} = 0.707$, $G_3/G_1 = 0.5$ [see Fig. 11 and Eqs. (69), (70)]

$$\frac{1}{2\pi i}\int_{\Gamma_1}\left\{(\phi^{(1)}(\varsigma)+\frac{\omega(\varsigma)}{\overline{\omega'(\varsigma)}}\overline{\phi'^{(1)}(\varsigma)}+\overline{\psi^{(1)}(\varsigma)})\right.$$
$$\left.-(\phi^{(2)}(\varsigma)+\frac{\omega(\varsigma)}{\overline{\omega'(\varsigma)}}\overline{\phi'^{(2)}(\varsigma)}+\overline{\psi^{(2)}(\varsigma)})\right\}\varsigma^{j-1}\mathrm{d}\varsigma=0\quad(j=-N,\ldots,-1,1,\ldots,N),\tag{71}$$

$$\frac{1}{2\pi i}\int_{\Gamma_1}\left\{\frac{1}{2G_1}(\kappa_1\phi^{(1)}(\varsigma)-\frac{\omega(\varsigma)}{\overline{\omega'(\varsigma)}}\overline{\phi'^{(1)}(\varsigma)}-\overline{\psi^{(1)}(\varsigma)})\right.$$
$$\left.-\frac{1}{2G_2}(\kappa_2\phi^{(2)}(\varsigma)-\frac{\omega(\varsigma)}{\overline{\omega'(\varsigma)}}\overline{\phi'^{(2)}(\varsigma)}-\overline{\psi^{(2)}(\varsigma)})\right\}\varsigma^{j-1}\mathrm{d}\varsigma=0\quad(j=-N,\ldots,-1,1,\ldots,N).\tag{72}$$

After using Eqs. (71) and (72), the transfer matrix for the continuity conditions for traction and displacement is therefore obtained. In fact, Eqs. (71) and (72) represent a kind of weight residue formulation, or a weaker formulation for the boundary conditions along the interface.

In fact, for example, if we expand the term $(\phi^{(1)}(\varsigma) + \frac{\omega(\varsigma)}{\overline{\omega'(\varsigma)}}\overline{\phi'^{(1)}(\varsigma)} + \overline{\psi^{(1)}(\varsigma)})$ in a Laurent series, the derivation for the continuity conditions shown by Eqs. (32) and (33) must be complicated. It is seen that the weaker formulation shown by Eqs. (71) and (72) is a particular advantage in the present paper.

Appendix A: Derivation of the transfer matrix from continuity conditions for traction and displacement along the interface

First of all, we define two particular integrals as follows:

$$I_1 = \frac{1}{2\pi i}\int_{\Gamma_1} \varsigma^{n-1}\mathrm{d}\varsigma, \qquad (n\text{-integer}) \tag{A.1}$$

$$I_2 = \frac{1}{2\pi i}\int_{\Gamma_1} \frac{\varsigma^n}{\varsigma^2 - q^2}\mathrm{d}\varsigma, \qquad (n\text{-integer}) \tag{A.2}$$

where Γ_1 denotes a circle with radius ρ_1, and "q" is a positive real value with property $q > \rho_1$ (Fig. 16).

Clearly, we have

$$I_1 = \frac{1}{2\pi i}\int_{\Gamma_1} \varsigma^{n-1}\mathrm{d}\varsigma = \delta_n \tag{A.3}$$

where

$$\delta_n = 1 \quad \text{for} \quad n = 0, \quad \text{and} \quad \delta_n = 0 \quad \text{for}\, n \neq 0. \tag{A.4}$$

In addition, we have [16]

$$I_2 = \frac{1}{2\pi i}\int_{\Gamma_1} \frac{\varsigma^n}{\varsigma^2 - q^2}\mathrm{d}\varsigma = \frac{1}{2\pi i}\int_{\Gamma_1} \frac{1}{2q}\left(\frac{1}{\varsigma - q} - \frac{1}{\varsigma + q}\right)\varsigma^n \mathrm{d}\varsigma = h_n(q)\Delta_n \tag{A.5}$$

where

$$h_n(q) = -\frac{1 - (-1)^n}{2}q^{n-1}, \tag{A.6}$$

$$\Delta_n = 1 \quad \text{for}\, n \leq -1, \quad \text{and} \quad \Delta_n = 0 \quad \text{for}\, n \geq 0. \tag{A.7}$$

Clearly, for the point $\varsigma \in \Gamma_1$, or $\varsigma = \rho_1 e^{i\theta}$, we have (Fig. 16)

$$\varsigma\overline{\varsigma} = \rho_1^2, \quad \text{or} \quad \overline{\varsigma} = \frac{\rho_1^2}{\varsigma}. \tag{A.8}$$

In addition, we define two complex potentials as follows:

$$\phi^{(1)}(\varsigma) = \sum_{k=-N}^{N} {}'a_k^{(1)}\varsigma^k, \quad \psi^{(1)}(\varsigma) = \sum_{k=-N}^{N} {}'b_k^{(1)}\varsigma^k \qquad (\varsigma = \rho e^{i\theta},\, \rho_o < \rho \leq \rho_1), \tag{A.9}$$

$$\phi^{(2)}(\varsigma) = \sum_{k=-N}^{N} {}'a_k^{(2)}\varsigma^k, \quad \psi^{(2)}(\varsigma) = \sum_{k=-N}^{N} {}'b_k^{(2)}\varsigma^k \qquad (\varsigma = \rho e^{i\theta},\, \rho_1 \leq \rho \leq \rho_2). \tag{A.10}$$

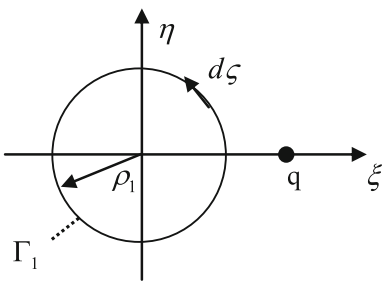

Fig. 16 A path Γ_1 for integration

By using Eqs. (A.3) and (A.9), we have

$$\frac{1}{2\pi i}\int_{\Gamma_1}\phi^{(1)}(\varsigma)\varsigma^{j-1}\mathrm{d}\varsigma=\frac{1}{2\pi i}\int_{\Gamma_1}\sum_{k=-N}^{N}{}'a_k^{(1)}\varsigma^{k+j-1}\mathrm{d}\varsigma=\sum_{k=-N}^{N}{}'\delta_{k+j}a_k^{(1)}, \tag{A.11}$$

After using Eqs. (4), (5), (A.8) and (A.9), along $\varsigma\in\Gamma_1$ or $\varsigma=\rho_1 e^{i\theta}$, we will find

$$\frac{\omega(\varsigma)}{\overline{\omega'(\varsigma)}}\overline{\phi'^{(1)}(\varsigma)}=-\frac{1}{\varsigma^2-q^2}\left(\frac{\rho_1^2}{m}\varsigma^2+\rho_1^2\right)\sum_{k=-N}^{N}{}'ka_k^{(1)}\rho_1^{2k}\varsigma^{-k},\quad\text{with}\quad q=\frac{\rho_1^2}{\sqrt{m}}. \tag{A.12}$$

In addition, by using Eqs. (A.5) and (A.12) we have

$$\begin{aligned}\frac{1}{2\pi i}\int_{\Gamma_1}\frac{\omega(\varsigma)}{\overline{\omega'(\varsigma)}}\overline{\phi'^{(1)}(\varsigma)}\varsigma^{j-1}\mathrm{d}\varsigma=&-\frac{\rho_1^2}{m}\sum_{k=-N}^{N}{}'k\,\rho_1^{2k}a_k^{(1)}h_{-k+j+1}(q)\Delta_{-k+j+1}\\&-\rho_1^2\sum_{k=-N}^{N}{}'k\,\rho_1^{2k}a_k^{(1)}h_{-k+j-1}(q)\Delta_{-k+j-1}.\end{aligned} \tag{A.13}$$

By using Eqs. (A.8) and (A.9), along $\varsigma\in\Gamma_1$ or $\varsigma=\rho_1 e^{i\theta}$, we have

$$\overline{\psi^{(1)}(\varsigma)}=\sum_{k=-N}^{N}{}'\rho_1^{2k}b_k^{(1)}\varsigma^{-k}, \tag{A.14}$$

$$\frac{1}{2\pi i}\int_{\Gamma_1}\overline{\psi^{(1)}(\varsigma)}\varsigma^{j-1}\mathrm{d}\varsigma=\frac{1}{2\pi i}\int_{\Gamma_1}\sum_{k=-N}^{N}{}'\rho_1^{2k}b_k^{(1)}\varsigma^{-k+j-1}\mathrm{d}\varsigma=\sum_{k=-N}^{N}{}'\rho_1^{2k}\delta_{-k+j}b_k^{(1)}. \tag{A.15}$$

Similarly, along $\varsigma\in\Gamma_1$ or $\varsigma=\rho_1 e^{i\theta}$ we will obtain

$$\frac{1}{2\pi i}\int_{\Gamma_1}\phi^{(2)}(\varsigma)\varsigma^{j-1}\mathrm{d}\varsigma=\sum_{k=-N}^{N}{}'\delta_{k+j}a_k^{(2)}, \tag{A.16}$$

$$\begin{aligned}\frac{1}{2\pi i}\int_{\Gamma_1}\frac{\omega(\varsigma)}{\overline{\omega'(\varsigma)}}\overline{\phi'^{(2)}(\varsigma)}\varsigma^{j-1}\mathrm{d}\varsigma=&-\frac{\rho_1^2}{m}\sum_{k=-N}^{N}{}'k\,\rho_1^{2k}a_k^{(2)}h_{-k+j+1}(q)\Delta_{-k+j+1}\\&-\rho_1^2\sum_{k=-N}^{N}{}'k\,\rho_1^{2k}a_k^{(2)}h_{-k+j-1}(q)\Delta_{-k+j-1},\end{aligned} \tag{A.17}$$

$$\frac{1}{2\pi i}\int_{\Gamma_1}\overline{\psi^{(2)}(\varsigma)}\varsigma^{j-1}\mathrm{d}\varsigma=\sum_{k=-N}^{N}{}'\rho_1^{2k}\delta_{-k+j}b_k^{(2)}. \tag{A.18}$$

It is known that the continuity condition for the traction and displacement along the interface Σ_1, or along Γ_1 in the mapping plane in Fig. 1, can be expressed as follows:

$$\phi^{(1)}(\varsigma)+\frac{\omega(\varsigma)}{\overline{\omega'(\varsigma)}}\overline{\phi'^{(1)}(\varsigma)}+\overline{\psi^{(1)}(\varsigma)}=\phi^{(2)}(\varsigma)+\frac{\omega(\varsigma)}{\overline{\omega'(\varsigma)}}\overline{\phi'^{(2)}(\varsigma)}+\overline{\psi^{(2)}(\varsigma)},\ (\varsigma\in\Gamma_1), \tag{A.19}$$

$$\frac{1}{2G_1}\{\kappa_1\phi^{(1)}(\varsigma)-\frac{\omega(\varsigma)}{\overline{\omega'(\varsigma)}}\overline{\phi'^{(1)}(\varsigma)}-\overline{\psi^{(1)}(\varsigma)}\}=\frac{1}{2G_2}\{\kappa_2\phi^{(2)}(\varsigma)-\frac{\omega(\varsigma)}{\overline{\omega'(\varsigma)}}\overline{\phi'^{(2)}(\varsigma)}-\overline{\psi^{(2)}(\varsigma)}\},\ (\varsigma\in\Gamma_1). \tag{A.20}$$

It is seen that the continuation conditions shown by Eqs. (A.19) and (A.20) are expressed in the continuous form, which is formulated along the interface $\varsigma\in\Gamma_1$ with $\varsigma=\rho_1 e^{i\theta}$ (Fig. 1). Now we want to convert two conditions in a discrete form. To this end, we can apply the following operator:

$$\frac{1}{2\pi i}\int_{\Gamma_1}\{\ldots\}\varsigma^{j-1}\mathrm{d}\varsigma,\quad(j=-N,-(N-1),\ldots,-2,-1,1,2,\ldots,N-1,N) \tag{A.21}$$

to both side of Eqs. (A.19) and (A.20). After making the mentioned operation, from Eqs. (A.19) and (A.20) we have

$$[\mathbf{M}_1]_{4\mathbf{N}\times 4\mathbf{N}}\{A_1\}_{4N} = [\mathbf{M}_2]_{4\mathbf{N}\times 4\mathbf{N}}\{A_2\}_{4N} \tag{A.22}$$

where the two vectors are defined by

$$\{A_1\}_{4N} = \{a_{-N}^{(1)}\, a_{-(N-1)}^{(1)} \cdots a_{-1}^{(1)}\, a_1^{(1)} \cdots a_{N-1}^{(1)}\, a_N^{(1)}\, b_{-N}^{(1)}\, b_{-(N-1)}^{(1)} \cdots b_{-1}^{(1)}\, b_1^{(1)} \cdots b_{N-1}^{(1)}\, b_N^{(1)}\}^{\mathrm{T}}, \tag{A.23}$$

$$\{A_2\}_{4N} = \{a_{-N}^{(2)}\, a_{-(N-1)}^{(2)} \cdots a_{-1}^{(2)}\, a_1^{(2)} \cdots a_{N-1}^{(2)}\, a_N^{(2)}\, b_{-N}^{(2)}\, b_{-(N-1)}^{(2)} \cdots b_{-1}^{(2)}\, b_1^{(2)} \cdots b_{N-1}^{(2)}\, b_N^{(2)}\}^{\mathrm{T}}. \tag{A.24}$$

In Eqs. (A.23) and (A.24), the vectors $\{A_1\}_{4N}$ and $\{A_2\}_{4N}$ are composed of the coefficients in the Laurent series expansion for the complex potentials $\phi^{(1)}(\varsigma)$, $\psi^{(1)}(\varsigma)$, $\phi^{(2)}(\varsigma)$, $\psi^{(2)}(\varsigma)$ shown by Eqs. (A.9) and (A.10), respectively.

From Eq. (A.22), we have

$$\{A_2\}_{4N} = [\mathbf{S}_{21}]_{4\mathbf{N}\times 4\mathbf{N}}\{A_1\}_{4N} \tag{A.25}$$

where

$$[\mathbf{S}_{21}]_{4\mathbf{N}\times\mathbf{N}} = [\mathbf{M}_2^{-1}]_{4\mathbf{N}\times 4\mathbf{N}}\,[\mathbf{M}_1]_{4\mathbf{N}\times 4\mathbf{N}}. \tag{A.26}$$

In Eq. (A.25), $[\mathbf{M}_2^{-1}]_{4\mathbf{N}\times 4\mathbf{N}}$ represents the inverse matrix of $[\mathbf{M}_2]_{4\mathbf{N}\times 4\mathbf{N}}$.

Appendix B: Asymptotic solution for a small crack in the inclusion

In the case of the remote stresses σ_x^{∞} and σ_y^{∞} (Fig. 17), for solving the inclusion problem we can assume the following complex potentials in the inclusion:

$$\phi^{(1)}(\varsigma) = fR\left(\varsigma + \frac{m}{\varsigma}\right), \quad \text{or } \phi^{(1)*}(z) = fz, \tag{B.1}$$

$$\psi^{(1)}(\varsigma) = gR\left(\varsigma + \frac{m}{\varsigma}\right), \quad \text{or } \psi^{(1)*}(z) = gz \tag{B.2}$$

where "f" and "g" are two real constants.

After using the mapping relation shown by Eq. (4), the complex potentials for the matrix in the mapping plane will be

$$\phi^{(2)}(\varsigma) = R\Gamma\varsigma + \sum_{k=0}^{\infty}\frac{c_k}{\varsigma^k}, \quad (c_k\text{—some real constant coefficients}), \tag{B.3}$$

$$\psi^{(2)}(\varsigma) = R\Gamma_1\varsigma + \sum_{k=0}^{\infty}\frac{d_k}{\varsigma^k}, \quad (d_k\text{—some real constant coefficients}) \tag{B.4}$$

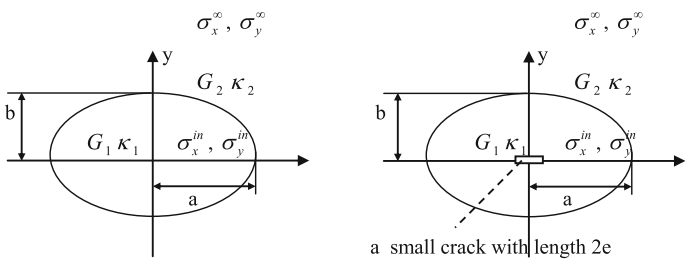

(a) **(b)**

Fig. 17 **a** An inclusion in an infinite matrix, **b** a small crack with length "2e"in the inclusion

where

$$\Gamma = \frac{\sigma_x^\infty + \sigma_y^\infty}{4}, \quad \Gamma_1 = \frac{\sigma_y^\infty - \sigma_x^\infty}{2}. \tag{B.5}$$

After using the displacement and traction continuity conditions along the elliptic interface, we can get an algebraic equation for "f" and "g," and the final solution is as follows [20]:

$$f = \frac{1}{4\Delta}\left\{(1-(1+m^2)\beta)(\sigma_x^\infty + \sigma_y^\infty) - 2m\beta(\sigma_y^\infty - \sigma_x^\infty)\right\}, \tag{B.6}$$

$$g = \frac{1}{4\Delta}\left\{-2m(1-\alpha-\beta)(\sigma_x^\infty + \sigma_y^\infty) + 2(\alpha+\beta)(\sigma_y^\infty - \sigma_x^\infty)\right\} \tag{B.7}$$

where

$$\alpha = \frac{G_2\kappa_1 + G_1}{G_1(1+\kappa_2)}, \quad \beta = \frac{G_1 - G_2}{G_1(1+\kappa_2)}, \tag{B.8}$$

$$\Delta = (\alpha+\beta)(1-\beta) - m^2\beta(2-\alpha-\beta). \tag{B.9}$$

From Eq. (1), we can evaluate the stress components in the inclusion (Fig. 17)

$$\sigma_x^{\text{in}} = 2f - g = \frac{1}{2\Delta}\left\{\left[1 + m(1-\alpha-\beta) - (1+m^2)\beta\right](\sigma_x^\infty + \sigma_y^\infty) - (\alpha+\beta+2m\beta)(\sigma_y^\infty - \sigma_x^\infty)\right\}, \tag{B.10}$$

$$\sigma_y^{\text{in}} = 2f + g = \frac{1}{2\Delta}\left\{\left[1 - m(1-\alpha-\beta) - (1+m^2)\beta\right](\sigma_x^\infty + \sigma_y^\infty) + (\alpha+\beta-2m\beta)(\sigma_y^\infty - \sigma_x^\infty)\right\}. \tag{B.11}$$

It is assumed that a small crack with length "$2e$" is placed in the comparatively large inclusion. In addition, we have the following stress intensity factor solution:

$$K_1 = \sigma_y^{\text{in}}\sqrt{\pi e}, \tag{B.12}$$

If we let $\sigma_x^\infty = p\sigma_y^\infty$, K_1 can be written in the form

$$K_1 = \delta\sigma_y^\infty\sqrt{\pi e} \tag{B.13}$$

where

$$\delta = \frac{1}{2\Delta}\left\{\left[1 - m(1-\alpha-\beta) - (1+m^2)\beta\right](1+p) + (\alpha+\beta-2m\beta)(1-p)\right\}, \tag{B.14}$$

In a particular case of the circular inclusion, or $a = b$ and $m = 0$, we have

$$\delta = \frac{1}{2\Delta}\{(1-\beta)(1+p) + (\alpha+\beta)(1-p)\} \tag{B.15}$$

where

$$\Delta = (\alpha+\beta)(1-\beta), \tag{B.16}$$

Clearly, Eq. (B.15) can be rewritten as

$$\delta = \frac{1}{2}\left\{\frac{1+p}{\alpha+\beta} + \frac{1-p}{1-\beta}\right\}. \tag{B.17}$$

The result shown by Eqs. (B.13) and (B.16) was first obtained in [17].

References

1. Eshelby, J.D.: The determination of the elastic field of an ellipsoidal inclusion and related problems. Proc. R. Soc. Lond. A **241**, 376–396 (1957)
2. Mura, T.: Micromechanics of Defects in Solids, 2nd ed. Martinus Nijhoff, Dordrecht (1987)
3. Gong, S.X.: A unified treatment of the elastic elliptical inclusion under antiplane shear. Arch. Appl. Mech. **65**, 55–64 (1995)
4. Ru, C.Q., Schiavone, P., Mioduchowcki, A.: Uniformity of stresses within a three-phase elliptic inclusion in anti-plane shear. J. Elast. **52**, 121–128 (1999)
5. Wang, X., Gao, X.L.: On the uniform stress state inside an inclusion of arbitrary shape in a three-phase composite. Z. Angew. Math. Phys. **62**, 1101–1116 (2011)
6. Chen, J.T., Wu, A.C.: Null-field approach for the multi-inclusion problem under antiplane shears. J. Appl. Mech. **74**, 469–487 (2007)
7. Chen, Y.Z.: Numerical solution of elastic inclusion problem using complex variable boundary integral equation. Acta Mech. **223**, 705–720 (2012)
8. Chen, Y.Z.: Solution for dissimilar elastic inclusions in a finite plate using boundary integral equation method. Int. J. Solids Struct. **49**, 1764–1772 (2012)
9. Zhu, L., Hoh, H.J., Wang, X., Keer, L.M., Pang, J.H.L., Song, B., Wang, Q.J.: A review of recent works on inclusions. Mech. Mater. **60**, 144–158 (2013)
10. Chen, T.: A confocally multicoated elliptical inclusion under antiplane shear: some new results. J. Elast. **74**, 87–97 (2004)
11. Y.Z. Chen: Closed-form solution for Eshelby's elliptic inclusion in antiplane elasticity using complex variable. Z. Angew. Math. Phys. **64**, 1797–1805 (2013)
12. Lam, K.Y., Ong, P.P., Wube, N.: Interaction between a circular inclusion and a symmetrically branched crack. Theor. Appl. Fract. Mech. **28**, 197–211 (1998)
13. Dong, S.Y., Lee, K.Y.: A new integral equation formulation of two-dimensional inclusion–crack problems. Int. J. Solids Struct. **42**, 5010–5020 (2005)
14. Chen, Y.Z., Chen, R.S.: Interaction between curved crack and elastic inclusion in an infinite plate. Arch. Appl. Mech. **67**, 566–575 (1997)
15. Cheeseman, B.A., Santare, M.H.: The interaction of a curved crack with a circular elastic inclusion. Int. J. Fract. **103**, 259–277 (2000)
16. Muskhelishvili, N.I.: Some Basic Problems of Mathematical Theory of Elasticity. Noordhooff, Groningen (1963)
17. Wu, C.H., Chen, C.H.: A crack in a confocal elliptic inhomogeneity embedded in an infinite medium. ASME J. Appl. Mech. **57**, 91–96 (1990)
18. Chen, Y.Z.: Transfer matrix method for the solution of multiple elliptic layers with different elastic properties. Part I: infinite matrix case. Acta Mech. (2015). doi:10.1007/s00707-14-1164.7
19. Chen, Y.Z., Hasebe, N., Lee, K.Y.: Multiple Crack Problem in Elasticity. WIT press, Southampton (2003)
20. Chen, Y.Z.: An innovative solution in closed form and numerical analysis for dissimilar elliptical inclusion in plane elasticity. Int. J. Appl. Mech. **6**, 1450080-1–1450080-16 (2014)